VISCOELASTIC EFFECTS IN LUBRICATED CONTACTS IN THE PRESENCE OF CAVITATION

A THESIS SUBMITTED TO

THE GRADUATE SCHOOL OF ENGINEERING AND SCIENCE

OF BILKENT UNIVERSITY

IN PARTIAL FULFILLMENT OF THE REQUIREMENTS FOR

THE DEGREE OF

MASTER OF SCIENCE

IN

MECHANICAL ENGINEERING

By

Samuel Shari Gamaniel

November 2020

VISCOELASTIC EFFECTS IN LUBRICATED CONTACTS IN THE PRESENCE OF CAVITATION
By Samuel Shari Gamaniel
November 2020

We certify that we have read this thesis and that in our opinion it is fully adequate, in scope and in quality, as a thesis for the degree of Master of Science.

Luca, Biancofiore(Advisor)

İlker, Temizer

Hacı Abdullah, Taşdemir

Approved for the Graduate School of Engineering and Science:

Ezhan Karaşan
Director of the Graduate School

ABSTRACT

VISCOELASTIC EFFECTS IN LUBRICATED CONTACTS IN THE PRESENCE OF CAVITATION

Samuel Shari Gamaniel
M.S. in Mechanical Engineering
Advisor: Luca, Biancofiore
November 2020

A model is proposed to study the influence of fluid viscoelasticity on the performance of lubricated contacts in the presence of cavitation. Previous studies on viscoelastic lubricants did not consider the presence of cavitation, rather reported negative pressures in regions where cavitation was expected to occur. The proposed model uses the Oldroyd-B constitutive model to describe the presence of cavitation and assumes that the Deborah number (De), the ratio between polymer relaxation time and flow time scale, is small. In doing so, the viscoelastic thin film equations can be linearised in a similar approach to what was pioneered by "Tichy, J., 1996, Non-Newtonian lubrication with the convected Maxwell model." The zeroth order solution in De corresponds to the Reynolds equation and has been modified to describe also the film cavitation through the mass-conserving Elrod-Adams model. We model several bearing configurations for the flow of viscoelastic lubricants using (i) a cosine/parabolic profile representing a journal bearing unwrapped geometry, and (ii) a pocketed profile to model a textured surface in lubricated contacts. Introducing viscoelasticity to the cavitating journal bearing decreases the length of the non-active (cavitation) region due to an increasing pressure distribution in the lubricant film. This results in an increase to the load carrying capacity with increasing De corroborating the beneficial influence of the polymers in fluid film bearings. The pocket profile is shown to either increase or decrease the load carrying capacity with increasing viscoelastic effects, depending on the location of surface texturing at the contact. An oscillating squeeze flow problem is modeled for viscoelastic lubricants between two flat plates with motion only at the top surface. A reduction in the load carrying capacity at larger values of De is observed as film reformation is seen to be retarded with increasing viscoelastic effects. As viscoelastic effects become stronger, the nonactive region is grows continuously until reaching a value of De beyond which a full film reformation does not occur upon the inception of cavitation. The

study is extended to a direct numerical simulations using the openFoam toolbox. A model that couples a solver for incompressible, isothermal, two phase flow with interaction between the phases and a solver for viscoelastic fluids is proposed. However, DNS are only valid for lower values of De as instabilities occur as a result of the non-linear coupling.

Keywords: Tribology, Thin films, Hydrodynamic lubrication, Viscoelasticity, Cavitation, Journal bearings, Surface texture, Squeezing.

ÖZET

YAĞLANMIŞ TEMASLARDA KAVİTASYON VARLIĞINDA VİSKOELASTİK ETKİLER

Samuel Shari Gamaniel
Makine Mühendisliği, Yüksek Lisans
Tez Danışmanı: Luca, Biancofiore
Kasim 2020

Viskoelastik yağlayıcılarla ilgili önceki çalışmalar da kavitasyonun varlığını dikkate almadı, bunun yerine kavitasyonun meydana gelmesinin beklendiği bölgelerde negatif basınçlar bildirdi. Önerilen model, kavitasyonun varlığını tanımlamak için Oldroyd-B kurucu modelini kullanır ve polimer gevşeme süresi ile akış süresi ölçeği arasındaki oran olan Deborah sayısının (De) küçük olduğunu varsayar. Bunu yaparken, viskoelastik ince film denklemleri, "Tichy, J., 1996, Non-Newtonian lubrication with the convected Maxwell model." öncülüğüne benzer bir yaklaşımla doğrusallaştırılabilir. De'deki sıfırıncı dereceden çözüm Reynolds denklemine karşılık gelir ve kütlenin korunduğu Elrod-Adams modeli aracılığıyla film kavitasyonunu da açıklamak için değiştirilmiştir. Viskoelastik yağlayıcıların akışı için çeşitli yatak konfigürasyonlarını (i) sarılmamış bir mil yatağını temsil eden bir kosinüs / parabolik profil ve (ii) yağlı kontaklardaki dokulu bir yüzeyi modellemek için cepli bir profil kullanarak modelliyoruz. Kavitasyonun olduğu mil yatağına viskoelastisite katılması, artan basınç dağılımı nedeniyle yağlayıcı filmdeki aktif olmayan (kavitasyon) bölgenin uzunluğunu azaltır. Bu, polimerlerin akışkan film yataklardaki yararlı etkisini doğrulayan De artışıyla yük taşıma kapasitesinde bir artışa neden olur. Cep profilinin artan viskoelastik etkilerle, temas noktasındaki yüzey tekstüre konumuna bağlı olarak yük taşıma kapasitesini artırdığı veya azalttığı gösterilmiştir. Sadece üst yüzeyde hareket olan iki düz plaka arasındaki viskoelastik yağlayıcılar için salınımlı bir sıkışma akış problemi modellenmiştir. Film reformasyonunun artan viskoelastik etkilerle geciktiğinden, büyük De değerlerindeki yük taşıma kapasitesinde bir azalma gözlemlenir. Viskoelastik etkiler güçlendikçe, aktif olmayan bölge, De değerine ulaşana kadar sürekli olarak büyür ve bunun ötesinde, kavitasyon başlangıcında tam bir film reformasyonu meydana gelmez. Çalışma, openFoam araç kutusu

kullanılarak doğrudan sayısal simülasyonlara genişletildi. Sıkıştırılamaz, izotermal, iki fazlı akış için bir çözücü ile fazlar arasındaki etkileşimi ve viskoelastik akışkanlar için bir çözücüyü birleştiren bir model önerilmektedir. Ancak, doğrusal olmayan bağlantının bir sonucu olarak kararsızlıklar oluştuğundan, DNS yalnızca düşük De değerleri için geçerlidir.

Anahtar sözcükler: Triboloji, İnce filmler, Hidrodinamik yağlama, Viskoelastisite, Kavitasyon, Muylu yatakları, Yüzey dokusu, Sıkma.

Acknowledgement

This would not have been possible without the contributions, teachings and support of a lot of people.

Foremost, I would like to express my deepest gratitude to my advisor Dr. Biancofiore who believed in me and gave this opportunity to learn from and work with him. During this period, Dr. Biancofiore showed his full support and confidence in my work and was always available whenever I needed his guidance. For this I am indeed grateful.

I would like to acknowledge the Turkish National Research Agency (TÜBITAK) for supporting this work under the project 117M434.

My sincere gratitude goes to the entire mechanical engineering department for the guidance and support throughout this endeavor. The FluidFrame research group has shown immense support to me during this period. I have enjoyed my time with the group and had the opportunity to learn a lot from each one of you. I am thankful for the good memories and for making the office a good working environment.

My appreciation also extends to my friends for their kindness and motivation. Looking forward to many more years of good friendships. To my dear siblings who have always made me laugh even at difficult times, you have been a source of inspiration. I am grateful that I have you in my life.

I am grateful to my parents for their unending support and for always checking up on me within this period. Without them none of this could have ever been possible and for that I will remain eternally grateful. God bless you!

Finally, I will like to give all thanks to God for making all of this possible.

Contents

List of Figures

List of Tables

Chapter 1

Introduction

In moving machine parts, friction and wear reduction constitute a very significant problem in improving the efficiency and preserving the lifespan of surfaces in motion. Large amounts of energy is lost to friction in moving parts. Car engines lose approximately 7.5% of the generated power from fuel combustion while overcoming friction [3]. A common practice for reducing friction and mechanical wear in moving parts has been the introduction of lubricants. These lubricants are also useful in reducing the heat generated due to friction. Lubricant films are situated between moving parts to ensure a gap remains at these contacts. Lubricants work by exerting very high pressures capable of supporting the load of solid surfaces in relative motion, thus reducing friction, preventing contact and essentially minimizing wear.

Bearings are essential components that facilitate the smooth relative motion of two surfaces by acting to minimize friction and wear. They also ensure there is no undesired relative motion between machine parts by constraining the motion to only what is required. Lubricants have become useful in bearings and the study of the behavior of these lubricants in bearings has become necessary for designing more energy efficient machine parts. Bearing lubricants could either be a free flowing oil or a grease which is a combination of oil and a thicker base material. In this study, we shall focus on the oil based lubricants which provides the excellent lubrication performance and has flow properties that are easier to model.

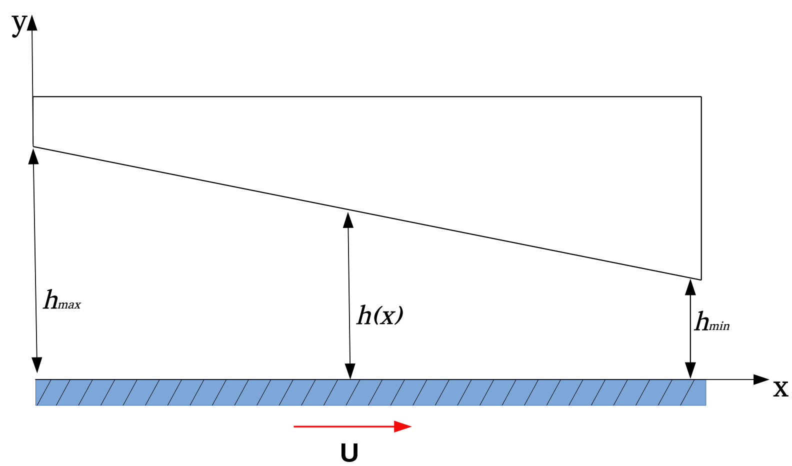

Figure 1.1: Schematic drawing of a plane slider bearing.

1.1 Lubricant films in bearings

The term fluid film bearings is used to describe a continuous fluid film separating bearing surfaces in relative motion [4]. Depending on the mode of operation, these can be further characterized into hydrostatic lubrication, hydrodynamic lubrication or elasto-hydrodynamic lubrication. In *hydrostatic lubrication* the lubricant film is pressurized from an external source. These mostly experience low friction and can carry larger loads making the excellent lubricants. However, hydrostatic lubrication requires the use of an external source of pressurized lubricant supply for its operation. *Hydrodynamic lubrication* does not operate with an external pressure gradient, instead the lubricant between the solid surfaces is dragged by the sliding motion of the surfaces leading to a pressure gradient dependent on the shape and slope of the surfaces. The hydrodynamic bearings, which will be the main focus of this thesis, are usually used in supporting the load of rotating shafts. One example is the thrust pad plane slider bearing shown in Fig. 1.1. *Elastohydrodynamic lubrication* refers to hydrodynamic lubrication occurring in lubricant films where elastic deformation is expected.

Understanding how lubricants in bearings operate involves studying the flow properties at key areas where certain phenomena are expected to be observed. At the high pressure regions, the lubricant behaves like a solid and exhibits properties that are different from what is observed in the bulk. These include the load capacity at the narrow gap in the region of minimum film thickness that ensures a separation of the surfaces whereas cavitation at the diverging region of the shaft that leads to the formation of high pressure bubbles which in extreme cases may damage the surfaces during bubble collapse.

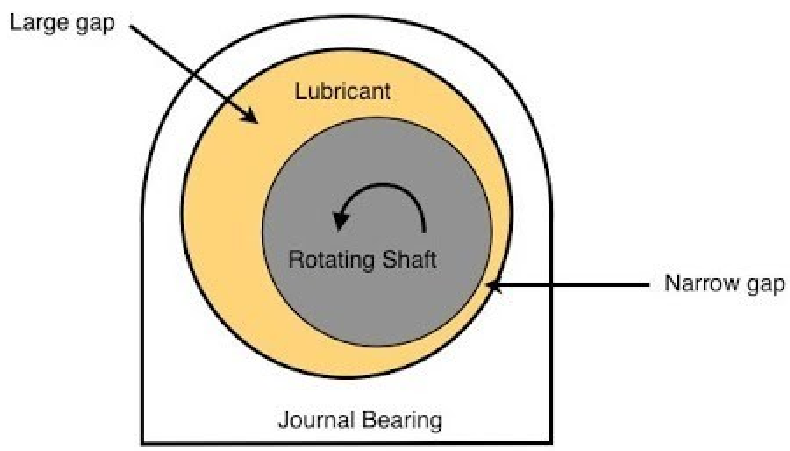

Figure 1.2: Schematic drawing of a journal bearing.

Lubricants may also contain additives which work to improve the bearing performance. Some additives can function as detergents that prevent particles from settling in the lubricant film or as dispersants that prevent the formation of larger particles in the film. Addition of polymer additives to mineral oils has become a common technique to improve the performance of lubricants. This practice was initially performed to minimize the temperature dependence of viscosity but it was observed to improve the lubricant characteristics when compared to other Newtonian lubricants [5, 6]. Lubricants with polymer additives present viscoelastic effects. Thus, their mechanical properties change and can no longer be treated as the regular Newtonian lubricants.

The prediction of the inception and presence of cavitation is an important factor in accurately describing the lubrication problem. Cavitation, which is a very common phenomenon in lubricated machine parts, describes the process of formation of vapor bubbles in a liquid which occurs due to a sudden decrease in local pressure usually below the saturation pressure. The liquid-vapor mixture regions can be observed at locations where the contact geometry diverges often imposing sub-ambient pressures within the lubricant.

The cavitation phenomenon has several practical applications which results from its devastating effects to machine elements including excessive noise and damage to propellers and pumps, coastal erosion and machine wear. However, there exist also several applications where cavitation becomes a wanted phenomenon some of which are in the homogenization of liquids, jets spray efficiency and in its applications to cleaning fluids.

In this thesis the main focus will be on the study of viscoelastic lubricants in bearing configurations where cavitation is expected to occur as a result of sudden drop in pressure within the lubricant film. One example is cavitation, expected to occur at the diverging section of the journal bearing shown in Fig. 1.2. Cavities may also form in regions of asperities or micro-roughness (surface textures) and in lubricant films that undergo oscillatory motions particularly in the negative squeezing regime (separation of bearing surfaces) that has been shown to result in the formation of liquid vapor mixture regions. We shall study the effects of viscoelasticity in lubricant films and consider the presence of cavitation in several bearing configurations where lubricants have been shown to undergo cavitation.

1.2 Literature review of lubricant modeling

Lubrication modeling started as early as 1886, Osborne Reynolds formulated the governing equations that describe the flow of a lubricant film along with several analytical solutions which pioneered the lubrication theory [7]. The classical Reynolds equation has become a fundamental basis in modeling the theories of lubrication.

1.2.1 Viscoelastic lubricants

Several numerical approaches were previously developed to describe the behavior of viscoelastic lubricants. Working with the upper convected Maxwell (UCM) model, Tichy et al. [8] carried out a regular perturbation analysis with the Newtonian lubrication solution as the leading order term. He reported that the flow profile i.e. curvature and slope, are critical factors in determining the load increment/reduction properties of viscoelastic lubricants. Li et al. [9] followed a similar approach and found that fluid viscoelasticity was the key factor in the improved lubricant pressure and the beneficial performance of lubricants observed during experiments. A nonlinear model able to incorporate various rheological models using the generalized Reynolds equation for non-Newtonian fluids, was developed by Wollf et al. [10]. Their findings were contrary to other linearized models as they reported that viscoelastic effects did not increase the load but instead reduced the load in a rolling contact. Their model however had failed to take into consideration the normal stress. More recently, a model able to predict the behavior of viscoelastic lubricants more accurately at large De compared to the generalized Reynolds equation has been developed by Ahmed et al. [11].

Phan-Thien and Tanner investigated the behavior of the Oldroyd-B constitutive model in squeeze flows [12]. They found that the load decreases as soon as De increases. This was later confirmed by Phan-Thien et al. [13] who developed an analytical solution while working still on squeeze flows and modeling the lubricant with the Oldroyd-B model. This finding did not match with experimental results [14]. To address this discrepancy, Phan-Thien et al. [15] updated their pioneering Phan Thien Tanner (PTT) model [16] to include the stress overshoot. Working with this new Modified Phan Thien Tanner (MPTT) model the load carrying capacity of the lubricant increases with increasing viscoelastic effects, showing the importance of the polymer stress overshoot. At very high shear rates, this stress overshoot can become very significant strengthening the description of the synovial fluid as an excellent lubricant [17, 18].

1.2.2 Cavitation

The first model to take cavitation into account is the so called 'half-Sommerfeld' condition by Gümbel [19] who accounted for the film rupture by setting the pressure equal to the cavitation pressure in the cavitation (non-active) region, however this model failed to consider the possibility of film reformation. Works by Swift and Steiber [20, 21] birthed the Swift-Steiber conditions that established a more adequate film rupture location. However, they were still unable to accurately and elaborately predict the lubricant film reformation. Jakobsson and Olsson [22, 23] pioneered a set of boundary conditions for the classic Reynolds equation, which are now generally termed the Jakobsson Floberg Olsson (JFO) theory. Elrod [24] solved a generalized form of the Reynolds equation incorporating the JFO theory in a numerical algorithm for hydrodynamic lubrication in the presence of cavitation. This has become a commonly used and widely accepted formulation known as the mass conserving Elrod-Adams model.

More in general many studies can be found on modeling cavitation in lubricated contacts but no one was assuming that the fluid is viscoelastic. Our main goal in this thesis is to fill this specific gap. To do so, we shall investigate the properties of viscoelastic thin film lubricants using the Oldroyd-B model in the presence of cavitation. This model is not just restricted to the field of tribology but has been used in a wide range of viscoelastic modeling including falling liquid films by Saprykin et al. [25] and blood transport modeling in biological systems by Anand et al. [26]. To do so, we linearize the governing equations using the Deborah number as the perturbation parameter. To predict the presence of cavitation in the contacts, this study uses a modified version of the Reynolds equation based on the Elrod-Adams formulation. In this way we can remove the pressure contribution of the mass flow at the cavitation region, preserve the conservation of mass and have a single equation that is applicable to both the full-film and cavitation regions. For squeezing problems, the mass conserving Elrod-Adams algorithm was reported to be much more accurate than the half-sommerfeld in predicting the behavior of lubricants when cavitation is present [2]. A new set of boundary conditions are proposed to accommodate for the changes that may occur at the film rupture locations due to the viscoelastic properties of the lubricants.

1.3 Thesis layout

This thesis is structured as follows. In chapter 2 we introduce a general cavitation model based on the Reynolds equation and the Elrod Adams algorithm for compressible and incompressible lubricants in roller bearings. This is followed by a model for viscoelastic lubricants in chapter 3. The model is introduced for lubricants where cavitation is unaccounted for and is extended to a more robust model that accounts for the presence of cavitation. In chapter 4 the results are presented for the viscoelastic models using (i) a parabolic slider representing an unwrapped journal bearing, (ii) a pocket slider mimicking a micro-textured surface profile, and (iii) the oscillating squeeze flow of two flat plates with the bottom surface held constant and the top surface moving in an oscillatory pattern. Chapter 5 proposes a direct numerical simulation solver for an incompressible, isothermal, two phase flow where the fluid is considered to be viscoelastic. Finally in chapter 6 conclusions are made and the prospects for future developments to the models are discussed.

Chapter 2

Cavitation in slider bearings

Cavitation describes the formation of gas bubbles in a liquid which occurs due to a sudden decrease in local pressure usually below the saturation pressure. Cavitation is a very common phenomenon in lubricated machine parts and fluid submerged moving devices and can be observed in regions where the contact geometry diverges often imposing sub-ambient pressures within the lubricant. The low pressures result in liquid-vapor mixture phases of the lubricant and the study of the formation of these vapor bubbles has led to the proposal of various cavitation models.

The current study focuses on developing a numerical formulation to predict the formation and growth of cavitation bubbles in lubricated contacts. The Reynolds equation through an algorithm based on the Elrod-Adams formulation implements the cavitation boundary conditions which is applied at the rupture and reformation locations of the film. Previous works in literature have considered cavitation using both theoretical models [1, 27, 28] and DNS [29, 30], here we shall focus on the theoretical models that describe the lubrication problem when cavitation is present.

This chapter is structured as follows; in section 2.1 the Reynolds equation for lubricant films is derived by simplifying and making some assumptions to the governing equations. This is followed by the introduction of the cavitation equation in section 2.2, alongside some compressible and incompressible models for cavitation. Finally results for the Reynolds equation for lubricant films using the different models presented are reported in section 2.3.

2.1 The Reynolds equation

The classical Reynolds theory of lubrication can be obtained by making several assumptions which are used in simplifying the Navier-Stokes equations. The Reynolds theory is based on making the observation that the lubricant may be treated as being iso-viscous, laminar and having a negligible curvature (almost parallel). The Reynolds theory of lubrication can then be initiated by making the following assumptions:

(1) The continuum description is valid
(2) The Navier-Stokes equations hold
(3) Compressibility is ignored
(4) The viscosity is ignored
(5) The film is thin and so therefore the flow is laminar and effects of inertia are negligible.

The lubricant compressibility effects can be introduced by making adjustments to the formulation. This will be done in the forthcoming sections by introducing concepts such as the bulk modulus and the Dowson Higginson expression for lubricant compressibility. The governing equations are

i. Continuity equation

$$\nabla \cdot \boldsymbol{u} = 0, \tag{2.1}$$

ii. Momentum equation

$$\rho \left(\frac{\partial \boldsymbol{u}}{\partial T} + \boldsymbol{u} \cdot \nabla \boldsymbol{u} \right) = -\nabla P + \eta \nabla^2 \boldsymbol{u} + \nabla \cdot \boldsymbol{\tau}, \tag{2.2}$$

where $\mathbf{u}(u_1, u_2, u_3)$ is the velocity vector, T is time, ρ is the density, P is the pressure, $\boldsymbol{\tau}$ is the stress tensor, and η is the viscosity. Assumptions (1)-(5) are applied to the governing equations, this results in a simplified momentum equation which can be integrated using the boundary conditions for velocities in the x_1 and z_1 directions following the footsteps of Szeri [4]. This simplification yields the velocity distribution:

$$u_1 = \frac{1}{2\eta}\frac{\partial P}{\partial x_1}\left(x_2^2 - x_2 H\right) + \left(1 - \frac{x_2}{H}\right) U_1 + \frac{x_2}{H} U_2 \text{ and} \tag{2.3}$$

$$u_3 = \frac{1}{2\eta}\frac{\partial P}{\partial x_3}\left(x_2^2 - x_2 H\right), \tag{2.4}$$

where U_1 and U_2 are the sliding velocities of the bottom and top surfaces respectively. Integrating the continuity equation across the film simplifies the problem as the averaged equation contains the x_2 component of velocity u_2 only at its boundary values which are presumed to be known. This integration yields

$$u_2 = -\int_0^{H(x_1,t_1)} \frac{\partial u_1}{\partial x_1} dx_2 - \int_0^{H(x_1,t_1)} \frac{\partial u_3}{\partial x_3} dx_2 . \tag{2.5}$$

Expressions for u_1 and u_3 are substituted into Eq. 2.5 making it possible to evaluate the integrals. It should be taken into account that

$$u_2 = -(V_1 - V_2) = dH/dt_1, \tag{2.6}$$

where V_1 and V_2 are the velocities of the top and bottom surfaces respectively as they approach each other. These equations lead to the generalized Reynolds equation for lubricant pressure which is expressed as:

$$\frac{\partial}{\partial x_1}\left(\frac{H^3}{\eta}\frac{\partial P}{\partial x_1}\right) + \frac{\partial}{\partial x_3}\left(\frac{H^3}{\eta}\frac{\partial P}{\partial x_3}\right) = 6\left(U_1 - U_2\right)\frac{\partial H}{\partial x_1} + 6H\frac{\partial\left(U_1 + U_2\right)}{\partial x_1} + 12\left(V_2 - V_1\right) \tag{2.7}$$

The generalized Reynolds equation for lubricant pressure (Eq. 2.7) can be further simplified by making the following assumptions that are valid for the lubricant flows described:

1. *The inertia terms are negligible,*
2. *The pressure gradient in the direction of the film thickness is negligible,*
3. *The fluid is Newtonian,*

4. Viscosity has a constant value,

5. No slip at liquid-solid boundary,

6. Angle of inclination is neglected for the coordinate system,

7. Flow is incompressible,

8. Relative tangential velocity only in x-direction,

9. Surfaces are rigid, and

10. Only one of the surfaces slides.

Applying these assumptions towards the simplification of Eq. 2.7 the two dimensional steady state form of the Reynolds equation for lubricant pressure can now be obtained as:

$$\frac{\partial}{\partial x_1}\left(H^3\frac{\partial P}{\partial x_1}\right)+\frac{\partial}{\partial x_3}\left(H^3\frac{\partial P}{\partial x_3}\right)= 6\eta\left(U\frac{\partial H}{\partial x_1}+H\frac{\partial u_1}{\partial x_1}\right) \tag{2.8}$$

where the single velocity term U is now used only for the velocity of the sliding surface.

2.2 Cavitation equation

The cavitation model described in this thesis follow the Elrod-Adams algorithm [24] which incorporates the Jakobsson-Floberg-Olsson (JFO) theory [22] with the following key objectives;

- To remove the pressure contribution of the mass flow in the cavitation region.
- Preserve the conservation of mass.
- Set approximately correct conditions at the cavitation boundaries.
- Produce a single equation applicable to both the full film and cavitated regions.
- Introduce a proper finite difference scheme for the governing equation.

The two dimensional transient form of Reynolds equation for a Newtonian lubricant in laminar flow that allows for the implementation of compressiblity effects can be expressed as [31]

$$\frac{\partial \rho H}{\partial T} + \frac{\partial}{\partial x_1}\left(\frac{\rho H U}{2} - \frac{\rho H^3}{12\eta}\frac{\partial P}{\partial x_1}\right) + \frac{\partial}{\partial x_3}\left(\frac{\rho H^3}{12\eta}\frac{\partial P}{\partial x_3}\right) = 0, \tag{2.9}$$

where the first term represents the squeezing of the lubricant, the second expression is the shear flow term and the third term represents the pressure induced flow of the lubricant.

2.2.1 Bulk modulus compressible model

The bulk modulus of a liquid is the ratio of its change in pressure to fractional volume compression. That is, the amount of pressure required to change a unit volume of a liquid. The reciprocal of the bulk modulus is called the compressibility of the substance. In the present context, it relates the density of a lubricant to the pressure at that location [31]. Lubricants with a larger bulk modulus will require a higher pressure to compress a unit volume of the lubricant compared to one with a lesser bulk modulus value. The pressure-density relation for the bulk modulus compressibility model is given as

$$\beta = \rho \frac{\partial P}{\partial \rho}. \tag{2.10}$$

A non-dimensional density term can then be introduced in the form

$$\theta = \frac{\rho}{\rho_c}, \tag{2.11}$$

where ρ_c is the density of the lubricant in the region of cavitation. Additionally, a switch function (g) is introduced into the pressure density relation to retain a constant cavitation pressure at the liquid-vapor mixture region ensuring shear flow dominance at that location. The switch function takes a value $g = 1$ in the full-film region and a value $g = 0$ in the cavitated region where the pressure induced flow term is expected to vanish. This switch function can now be introduced into the pressure density relation given in Eq. 2.10 as

$$g\beta \;=\; \rho\frac{\partial P}{\partial \rho} \;= \theta\,\frac{\partial P}{\partial \theta}. \tag{2.12}$$

Integrating Eq. 2.12 yields a direct pressure, density relationship

$$P \;=\; P_c + g\beta\, ln\theta. \tag{2.13}$$

Using Eq. 2.10 and Eq. 2.12, a new form of the Reynolds equation for cavitating lubricants can be derived from Eq. 2.9. With this a single cavitation equation for both regions within the film can be expressed as

$$\frac{\partial \rho_c H\theta}{\partial T} + \frac{\partial}{\partial x_1}\left(\frac{\rho_c HU}{2}\theta \;-\; \frac{\rho_c\beta H^3 g}{12\eta}\,\frac{\partial \theta}{\partial x_1}\right) + \frac{\partial}{\partial x_1}\left(-\frac{\rho_c\beta H^3 g}{12\eta}\frac{\partial \theta}{\partial x_3}\right) = 0. \tag{2.14}$$

In the region of cavitation where the switch function takes the value $g = 0$, Eq. 2.12 and Eq. 2.14 become

$$P \;=\; P_c \text{ and,} \tag{2.15}$$

$$\frac{\partial \rho_c H\theta}{\partial T} + \frac{\partial}{\partial x_1}\left(\frac{\rho_c HU\theta}{2}\right) = 0. \tag{2.16}$$

The constant bulk modulus introduced here is sometimes used in modeling the compressibility of the lubricants. However, in ideal lubricants the bulk modulus varies with the density of the fluid within the channel, making the constant bulk modulus expression only valid for a limited pressure range. Although using the bulk modulus as a constant also does produce good results within some acceptable pressure range, it is important to use an improved compressible model for the lubricant. To address this shortfall of the bulk modulus model, the Dowson Higginson term has been introduced. In the next section we shall introduce this more realistic model for compressible lubricants with cavitation present.

2.2.2 Dowson Higginson model

The Dowson Higginson expression is a compressibility relation for an experimentally measured mineral oil. This relation is given as

$$\theta = \frac{C_1 + C_2(P - P_c)}{C_1 + (P - P_c)}, \tag{2.17}$$

where the constant coefficients $C_1 = 0.59 \cdot 10^9$ and $C_2 = 1.34$ were derived from the measured data for a mineral oil [32]. The Reynolds equation in the form presented in Eq. 2.9 can obey an arbitrary compressibility relation for the lubricant and therefore the use of some measured experimental data is acceptable. In the Dowson Higginson expression (Eq. 2.17), P is a function of θ and so therefore the chain rule can be applied on the pressure gradient

$$\nabla P = \frac{dP}{d\theta}\, \nabla\theta. \tag{2.18}$$

Eqs. (2.9, 2.11, and 2.18) are solved to obtain a final form of the Reynolds equation for the Dowson Higginson expression.

$$\frac{U}{2}\frac{\partial(\theta H)}{\partial x_1} = \nabla \cdot \left(\frac{\theta\, H^3}{12\eta}\, g\, \frac{\partial P}{\partial \theta}\, \nabla\theta \right). \tag{2.19}$$

2.2.3 Incompressible Reynolds equation taking the bulk modulus at infinity

In the bulk modulus cavitation model discussed in section 2.2.1, the bulk modulus was introduced as an expression to define the compressibility of the lubricant. In the previous bulk modulus model, we could not assume that the liquid is incompressible by assuming a very large bulk modulus as this leads to numerical instabilities. Taking the bulk modulus to very large numbers and subsequently infinity, the assumption of incompressibility for that substance from the definition of the bulk modulus is valid. That approach is what has become the basis on which this derivation for an incompressible lubricant is developed. Starting from the Elrod-Adams algorithm [33], the generalized Reynolds equation for cavitation problems will be solved for the special case where incompressibility is modeled taking the bulk modulus to infinity.

To begin this formulation, the constant bulk modulus model for lubricant compressibility given in section 2.2.1 serves as a good starting point. The expression relating the bulk modulus β, to the pressure, P, and density ρ is given as [27]

$$\beta = \rho \frac{\partial P}{\partial \rho}, \tag{2.20}$$

which can be integrated to obtain;

$$P = P_c + \beta log(\frac{\rho}{\rho_c}). \tag{2.21}$$

Introducing the non-dimensional density term $\theta = \rho/\rho_c$ into this formulation and the expression for the bulk modulus at infinity $\beta = 1/\epsilon$. Here ϵ is a very small number going to $\epsilon = 0$ as the bulk modulus β goes to infinity. From Eq. 2.21

$$\theta \ = \ e^{(p-p_c)\epsilon}, \tag{2.22}$$

$$\theta \ = \ 1 + \frac{\partial \theta}{\partial \epsilon}_{\epsilon=0} \epsilon \ + \ o\left(\epsilon^2\right), \tag{2.23}$$

$$\frac{\partial \theta}{\partial \epsilon}_{\epsilon=0} = e^{(P-P_c)\epsilon}[\epsilon P + (P-P_c)] = e^{(P-P_c)\epsilon}[\epsilon \frac{\partial P}{\partial \epsilon} + (P-P_c)]_{\epsilon=0} = P - P_c \text{and}, \tag{2.24}$$

$$\theta = 1 + (P - P_c)\epsilon. \tag{2.25}$$

The lubricant incompressibility assumption that bulk modulus is at infinity is valid only at the full-film region and thus the derived expression is used only in the full-film region of the cavitation equation. The new model is derived from the bulk modulus cavitation equation [33]

$$\frac{\partial}{\partial x_1}\left(\frac{HU\theta}{2} - \frac{\beta H^3}{12\eta}\frac{\partial \theta}{\partial x_1}\right) = 0. \tag{2.26}$$

Coupling Eq. 2.25 and Eq. 2.26 yields a Reynolds equation of the form

$$\frac{U}{2}\frac{H}{x_1}\theta + \frac{\partial \theta}{\partial x_1}\frac{Hu_1}{2} - \frac{1}{\epsilon}\frac{H^3}{12\eta}\frac{\partial^2 \theta}{\partial x_1^2} - \frac{1}{6\eta\epsilon}\frac{\theta}{\partial x_1}H^2\frac{\partial H}{\partial x_1}, \tag{2.27}$$

where

$$\frac{\partial \theta}{\partial x_1} = \frac{\partial P}{\partial x_1}\epsilon. \tag{2.28}$$

Eq. 2.28 can then be expressed as

$$\frac{1}{12\eta}\frac{\partial}{\partial x_1}\left(H^3\frac{\partial P}{\partial x_1}\right) - \frac{U}{2}\frac{\partial H}{\partial x_1} = \epsilon H\frac{\partial P}{\partial x_1} + \epsilon\frac{U}{2}\frac{\partial H}{\partial x_1}(P - P_c). \tag{2.29}$$

Taking the bulk modulus to infinity and consequently $\epsilon = 0$, the final form for the incompressible Reynolds equation is reached

$$\frac{1}{12\eta}\frac{\partial}{\partial x_1}\left(H^3\frac{\partial P}{\partial x_1}\right) = \frac{U}{2}\frac{\partial H}{\partial x_1}. \tag{2.30}$$

2.3 Preliminary results

In this section we introduce the (i) thrust pad bearing, and (ii) journal bearing configurations which will be considered for analysis. Firstly, the thrust pad bearing modeled using a plane slider bearing will be used to check the validity of the derived Reynolds equation without cavitation present (section 2.3.1). This will then be extended to a solution for the cavitation equations making use of a journal bearing which is modeled with a parabolic slider geometry (section 2.3.2). Cavitation has been shown to occur at the diverging end of the parabolic slider geometry.

Thrust bearings have flat surfaces which constrain the lubricant films whereas the journal bearings have a different (concentric) configuration. However, due to the large channel length compared to the film height, the curves become negligible and thus the parallel film assumption still holds.

2.3.1 Thrust pad bearing

To model the pressure distribution in the thrust pad bearing, a plane slider geometry with an inclined moving top surface is considered. The simplified two dimensional Reynolds equation for a plane slider with top surface moving at constant velocity U and the lubricant film having a constant viscosity η is obtained by simplifying Eq. 2.7 to obtain:

$$\frac{\partial}{\partial x_1}\left(H^3\frac{\partial P}{\partial x_1}\right) = 6\eta U\frac{\partial H}{\partial x_1}. \tag{2.31}$$

Table 2.1 lists the parameters for the plane slider geometry and the fluid properties used in the numerical simulations. At the inlet and exit of the channel, a pressure boundary condition $P(0) = P(L) = 0$ is set and an initial pressure boundary condition $P = 0$, is implemented throughout the lubricant film.

Configuration parameter	**Numerical value**	**Units**
Length L	10	mm
Min. height H_{min}	0.02	mm
Max. height H_{max}	0.04	mm
Velocity U	20	m/s
Viscosity η	10	mPa.s

Table 2.1: Dimensions and fluid properties for a plane slider bearing.

The results are obtained by considering $n = 100$ grid point locations on the x-axis. A finite difference scheme is applied to numerically obtain an approximate solution of the pressure distribution within the film. In particular, a central differencing numerical scheme was used. A Gauss Seidel iteration scheme was employed to ensure convergence of the pressure term, this error convergence criterion was determined using

$$\frac{\left|\sum_{i=1}^{n}(p_i)_{iteration\ k} - \sum_{i=1}^{n}(p_i)_{iteration\ k-1}\right|}{\left|\sum_{i=1}^{n}(p_i)_{iteration\ k}\right|} \leq tolerance, \tag{2.32}$$

where n and k are the number of nodes and iterations respectively. The tolerance for this simulation was set to 10^{-8}.

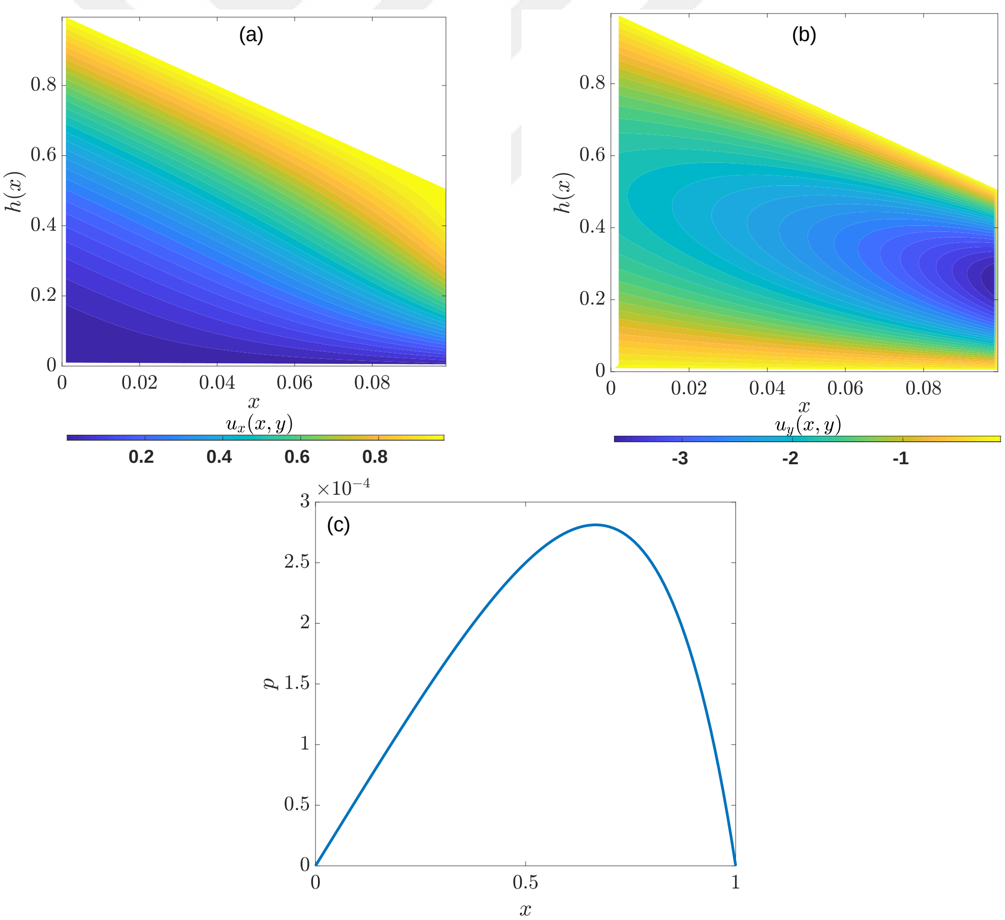

Figure 2.1: (a) u_x velocity distribution, (b) u_y velocity distribution and (c) pressure distribution in the plane slider bearing.

For consistency, we report the non-dimensional results where the non-dimensional terms have been introduced to our equations in the following manner

$$x = \tfrac{x_1}{L}, \qquad p = \tfrac{PC^3}{6\eta U L^2}, \qquad C = \tfrac{H_{max}-H_{min}}{2},$$

$$y = \tfrac{x_2}{H_{max}}, \qquad u_x = \tfrac{u_1}{U}, \text{ and} \qquad h(x) = \tfrac{H(x_1)}{H_{max}}.$$

Where L is the characteristic length along the film in the x-direction, H_{max} is the characteristic length across the film in the y-direction and U is the characteristic sliding velocity. The velocity profile also showing the configuration for the plane slider bearing can be seen in Fig. 2.1a which is the velocity in the x-direction and Fig. 2.1b for the velocity in the y-direction. The pressure distribution in the plane slider bearing is reported in Fig. 2.1c where all regions within the lubricant film have positive pressures indicating there is no region where cavitation is occurring.

2.3.2 Journal bearing

An unwrapped journal bearing is considered and modeled using a cosine slider geometry with its bottom surface kept constant and its top surface having a constant sliding velocity. This profile has been defined using

$$h\left(x\right) = \frac{h_{min}}{2} cos\left(\frac{2\pi x}{L}\right) + \frac{h_{max} + h_{min}}{2}. \tag{2.33}$$

A similar set of non-dimensional terms as has been introduced for the plane slider will be used in the journal bearing, the non-dimensional term for the pressure is updated as follows $p = \frac{P-P_c}{\eta U L/H_{max}^2}$, where the cavitation pressure P_c has been included to account for the presence of cavitation in the journal bearing. The cavitation pressure is set to the atmospheric pressure, $P_c = P_a = 10^5$MPa. An atmospheric boundary condition is imposed at the inlet and outlet boundaries ($P(0) = P(1) = P_a$).

The one dimensional steady state Reynolds cavitation equation for a Newtonian lubricant in laminar flow allowing for compressibility effects can be expressed as

$$\frac{\partial}{\partial x}\left(\frac{\rho_c hU}{2}\theta - \frac{\rho_c \beta h^3 g}{12\mu}\frac{\partial \theta}{\partial x}\right) = 0. \tag{2.34}$$

In the full-film region (g=1), this equation is an elliptic partial differential equation and thus the central difference scheme is applied such that the dependent variable at any point within the full-film depends on the neighboring point variable values. Whereas in the cavitated region (g = 0) the equation becomes hyperbolic and thus the downstream influences are not valid upstream and the forward finite difference scheme is applied. The implicit finite difference scheme was numerically applied to determine the film fraction distribution within the lubricant channel. All nodes were initially considered to be in the full-film regime and the Dirichlet type boundary conditions were taken for the film fraction θ which was set to be greater than 1 at the inlet and exit nodes.

Configuration parameter	**Numerical value**	**Units**
Length L	$7.62 * 10^{-2}$	m
Min. height H_{min}	$2.54 * 10^{-5}$	m
Max. height H_{max}	$5.08 * 10^{-5}$	m
Surf. velocity U	4.57	m/s
Viscosity η	0.039	Pa·s

Table 2.2: Dimensions and fluid properties for cosine slider bearing.

Using the Elrod-Adams algorithm for constant bulk modulus, the discretized equation is solved to obtain the fractional film content distribution. The parameters used in this particular configuration have been tabulated in table 2.2. The film fraction can be obtained by solving Eq. 2.34 iteratively setting an error convergence criterion after each iteration using Eq. 2.32. Similar to the previous configuration for the plane slider the tolerance is set to 10^{-8}. The pressure can be found for each iteration by converting the film fraction to the corresponding pressure distribution using Eq. 2.13. The lubricant film profile and velocity distribution for the cosine slider is shown in Fig. 2.2a for the component in the x-direction and Fig. 2.2b for the component in the y-direction respectively.

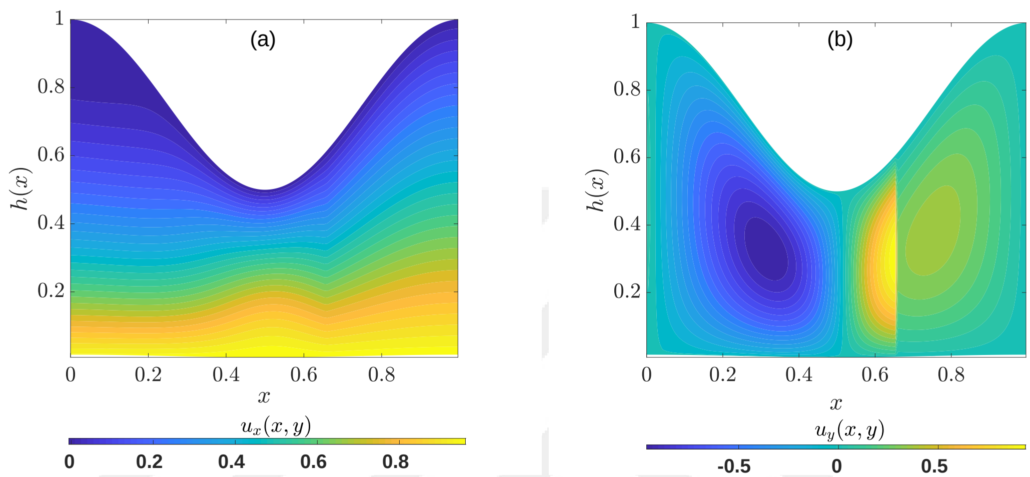

Figure 2.2: Velocity profile of a cosine slider showing the (a) x-component and (b) y-component of velocity.

The cavitation solution for the cosine slider bearing using the Dowson-Higginson model is reported and compared to the constant bulk modulus model. Compressibility effects will be studied over several values for the constant bulk modulus

Model	**Max. pressure**	**% of non-cavitated region**
BM = 0.069GPa	3.79Mpa	71%
BM = 2.4GPa	3.67Mpa	68%
Dowson Higginson	3.96Mpa	69%

Table 2.3: Maximum pressure and cavitation size for different models using a cosine slider.

and Dowson-Higginson parameters. These comparisons will highlight the influence of compressibility on the maximum pressure and region of cavitation. The corresponding values for the different models and parameters are shown in table 2.3.

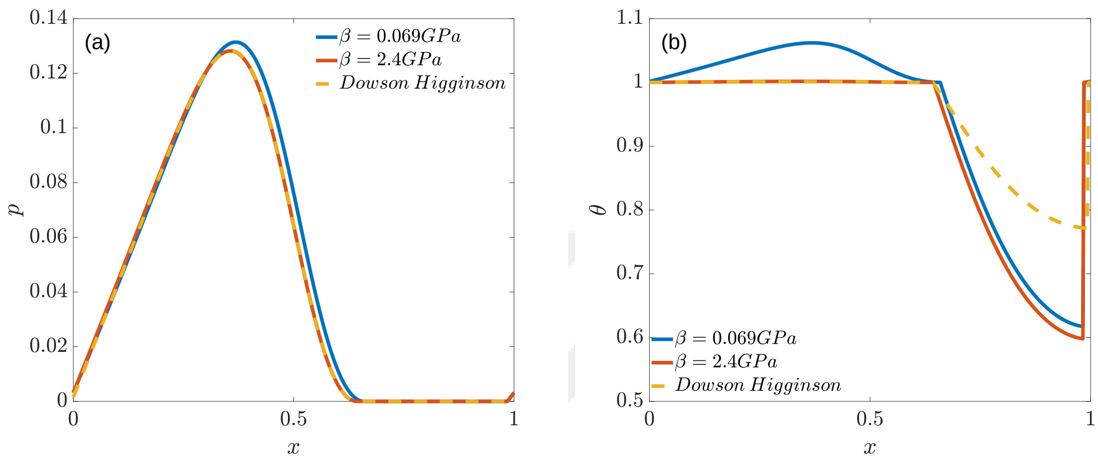

Figure 2.3: Lubricant pressure distribution and fluid film fraction comparing different models in a cosine slider.

The pressure distribution within the lubricant film for the cosine slider is shown in Fig. 2.3a. Results are compared for different parameters of the bulk modulus and Dowson Higginson model. We observe an decrease to the maximum pressure when β increases. Results indicate that a more compressible lubricant shows a decrease in the cavitation region. This can be confirmed from the corresponding fractional film content (θ) distribution reported in Fig. 2.3b. A higher bulk modulus value (less compressible lubricant) increases the cavitation region and vice versa.

Chapter 3

Viscoelastic lubrication with cavitation present

Viscoelastic lubricants exhibit different mechanical properties from conventional Newtonian lubricants and as such there is the need to modify the classical lubrication equations to consider viscoelasticity. Viscoelastic fluids exhibit a characteristic memory time scale, i.e. the characteristic relaxation time λ defined as the materials ratio of viscosity to its elastic modulus. The strength of viscoelastic effects can be measured by the Deborah number, defined as the ratio of the characteristic relaxation time to the process time or observation time, $De = \lambda/T$. At smaller relaxation times or conversely for longer observation times, the fluid is expected to behave as Newtonian whereas as soon as the Deborah number increases the fluid viscoelasticity cannot be neglected anymore.

In this section we discuss the mathematical model and the numerical algorithm used to describe the behavior of viscoelastic lubricants. Particularly in section 3.1, we introduce the governing equations and in section 3.2 we describe the contact geometries analyzed in this paper. We apply the thin film approximation to obtain a non-dimensional lower order set of equations in section 3.3. In section 3.4 these set of equations are linearized for solving a pure sliding motion and an oscillatory squeeze motion. This is followed by a derivation of the viscoelastic lubricant equation in section 3.5. In section 3.6 the cavitation problem is introduced into the viscoelastic equations. Afterwards, in section 3.7 we discuss the cavitation problem in detail and introduce a set of boundary conditions to capture the effect of viscoelasticity. Finally, in section 3.8 we make a detailed discussion on the numerical method and algorithm employed to solve the viscoelastic lubrication equations.

3.1 Governing equations

The governing equations for the isothermal flow of a viscoelastic fluid are given by

(i) Continuity equation

$$\frac{D\rho}{DT} + \rho\nabla\cdot\boldsymbol{u} = 0, \tag{3.1}$$

(ii) Momentum equation

$$\rho\left(\frac{\partial\boldsymbol{u}}{\partial T} + \boldsymbol{u}\cdot\nabla\boldsymbol{u}\right) = -\nabla P + \eta_s\nabla^2\boldsymbol{u} + \nabla\cdot\boldsymbol{\tau}, \tag{3.2}$$

(iii) Oldroyd-B constitutive equation

$$\boldsymbol{\tau} + \lambda\left(\frac{\partial\boldsymbol{\tau}}{\partial T} + \boldsymbol{u}\cdot\nabla\boldsymbol{\tau} - (\nabla\boldsymbol{u})\cdot\boldsymbol{\tau} - \boldsymbol{\tau}\cdot(\nabla\boldsymbol{u})^T\right) = 2\eta_p\mathbf{D}, \tag{3.3}$$

where ρ is the density, T is time, $\mathbf{u}(u_1, u_2)$ is the velocity vector, P is the pressure, $\boldsymbol{\tau}$ is the stress tensor, λ is the characteristic fluid relaxation time, η_s is the solvent viscosity, η_p is the polymer viscosity and $\mathbf{D}$ is the rate of deformation tensor expressed as

$$\mathbf{D} = \frac{1}{2}\left(\nabla\boldsymbol{u} + (\nabla\boldsymbol{u})^T\right). \tag{3.4}$$

Other types of constitutive equations can be used such as those for UCM model [8], PTT [16] or MPTT [15]. Particularly the MPTT constitutive equations is presented in Appendix A (see Eq. A.5).

In this formulation, we make the assumption that the liquid is incompressible and have therefore made use of the incompressible Oldroyd-B constitutive equation [34]. Note that as cavitation is expected to be present, the compressible Navier-Stokes equations are being employed to account for the compressibility of the vapor-mixture region.

3.2 Geometries

In this section, we introduce the contact geometries studied in this work.

1. Consider a 2-D thin film flow of a lubricant between two rigid surfaces with the top surface held constant and the bottom surface sliding at a constant velocity U in the horizontal x_1-direction as illustrated in Fig. 3.1. We assume no-slippage at the contact boundaries and the pressure at both channel inlet and outlet is atmospheric $P = P_a = 10^5$ Pa.

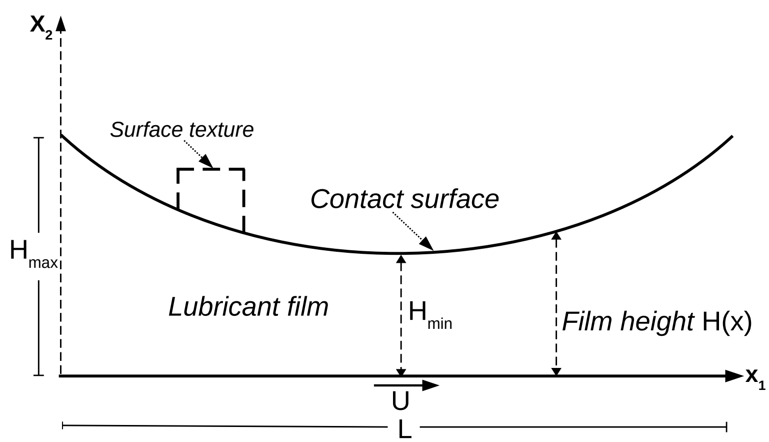

Figure 3.1: Schematic representation of the pure sliding thin film flow of a lubricant.

2. We consider the 2-D case of a lubricant between two flat plates, where the bottom plate is kept constant, whereas the top plate moves with an oscillatory velocity ($V = dH/dT$) only in the normal x_2-direction. A schematic diagram of this oscillatory squeeze film configuration is shown in Fig. 3.2.

In this thesis we study a flat oscillating surface, however it is possible to apply our model to other curved surfaces. The initial pressure is set to be the atmospheric pressure $P(0) = P_a = 10^5$ Pa.

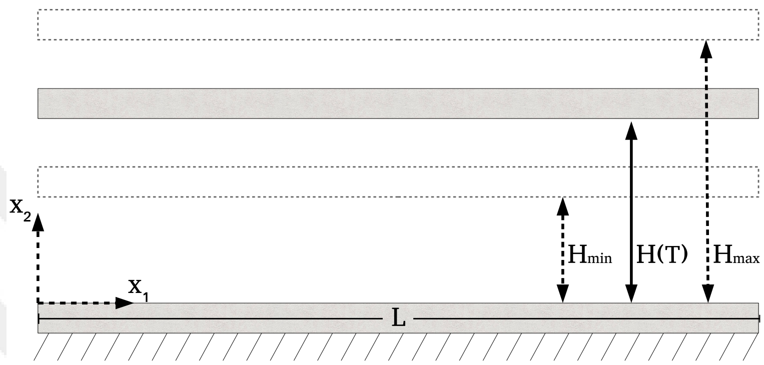

Figure 3.2: Schematic representation of the oscillating squeeze flow of a lubricant.

In both cases we use as (i) horizontal length scale the contact length L and (ii) vertical length scale the maximum height of the contact H_{max}. We assume that the lubricant cavitation pressure P_c is $P_c = 0$.

3.3 Thin film approximation

Following the footprints of Tichy et al. [8], a set of dimensionless variables are introduced to express the governing equations in non-dimensional form. The dimensionless quantities are

$$x = \frac{x_1}{L}, \qquad \tau_{xx} = \frac{\tau_{11}}{\eta U_{ref} L/H_{max}^2}, \qquad u_x = \frac{u_1}{U_{ref}}, \qquad \theta = \frac{\rho}{\rho_l},$$

$$y = \frac{x_2}{H_{max}}, \qquad \tau_{xy} = \frac{\tau_{12}}{\eta U_{ref}/H_{max}}, \qquad u_y = \frac{u_2}{U_{ref} H_{max}/L}, \qquad p = \frac{P - P_c}{\eta U_{ref} L/H_{max}^2},$$

$$\epsilon = \frac{H_{max}}{L}, \qquad \tau_{yy} = \frac{\tau_{22}}{\eta U_{ref}/L}, \qquad h(x,t) = \frac{H(x_1,T)}{H_{max}}, \qquad t = \frac{T U_{ref}}{H_{max}}, \text{ and}$$

$$De = \frac{\lambda U_{ref}}{H_{max}}.$$

In this formulation, it is assumed that the horizontal length scale is much larger than the vertical length scale: $L >> H_{max}$. As a result, the parameter ϵ is a very small number allowing us to make the thin film approximation. An elaborate formulation of the lubrication approximation detailing the expansion in ϵ is reported in Appendix B. We remember the fluid fraction term θ to be the non-dimensional density, where ρ_l is the density of the liquid. The velocity reference scale U_{ref} has been defined to describe the general motion of either a roller bearing or the squeeze flow problem

$$U_{ref} = \sqrt{U_{x,ref}^2 + \frac{U_{y,ref}^2}{\epsilon^2}}. \tag{3.5}$$

Introducing the non-dimensional quantities in Eqs. (3.1 - 3.3) and applying the lubrication approximation, the governing equations can be expressed as

$$\frac{\partial \theta}{\partial t} + \frac{\partial (\theta u_x)}{\partial x} + \frac{\partial (\theta u_y)}{\partial y} = 0, \tag{3.6a}$$

$$\frac{\partial \tau_{xx}}{\partial x} + \frac{\partial \tau_{xy}}{\partial y} + \beta \frac{\partial^2 u_x}{\partial y^2} = \frac{\partial p}{\partial x}, \tag{3.6b}$$

$$\frac{\partial p}{\partial y} = 0, \tag{3.6c}$$

$$\tau_{xx} + \epsilon De \left(\frac{\partial \tau_{xx}}{\partial t} + u_x \frac{\partial \tau_{xx}}{\partial x} + u_y \frac{\partial \tau_{xx}}{\partial y} - 2\frac{\partial u_x}{\partial y}\tau_{xy} - 2\frac{\partial u_x}{\partial x}\tau_{xx} \right) = 0, \tag{3.6d}$$

$$\tau_{xy} + \epsilon De \left(\frac{\partial \tau_{xy}}{\partial t} + u_x \frac{\partial \tau_{xy}}{\partial x} + u_y \frac{\partial \tau_{xy}}{\partial y} - \frac{\partial u_x}{\partial y}\tau_{yy} - \frac{\partial u_y}{\partial x}\tau_{xx} \right) = -(1-\beta)\frac{\partial u_x}{\partial y}, \text{ and} \tag{3.6e}$$

$$\tau_{yy} + \epsilon\, De \left(\frac{\partial \tau_{yy}}{\partial t} + u_x \frac{\partial \tau_{yy}}{\partial x} + u_y \frac{\partial \tau_{yy}}{\partial y} - 2\frac{\partial u_y}{\partial y}\tau_{yy} - 2\frac{\partial u_y}{\partial x}\tau_{xy} \right) = -2(1-\beta)\frac{\partial u_y}{\partial y}. \tag{3.6f}$$

Note that we introduced also the solvent concentration in terms of viscosity $\beta = \frac{\eta_s}{\eta_s+\eta_p}$. When $\beta = 1$ the lubricant is Newtonian. Unless explicitly stated otherwise, we assume that the lubricant is fully viscoelastic, consequently, the solvent concentration will be taken as $\beta = 0$.

3.4 Perturbation analysis

A regular perturbation expansion is applied to Eqs. (3.6a -3.6f) where the perturbation parameter is ϵDe. In this analysis the leading term will be the Newtonian lubrication solution marked with a superscript L, whereas the first order correction term is represented with a superscript D.

$$u_x = u_x^L + \epsilon De \cdot u_x^D + O(\epsilon^2 De^2), \tag{3.7a}$$

$$u_y = u_y^L + \epsilon De \cdot u_y^D + O(\epsilon^2 De^2), \tag{3.7b}$$

$$p = p^L + \epsilon De \cdot p^D + O(\epsilon^2 De^2), \tag{3.7c}$$

$$\theta = \theta^L + \epsilon De \cdot \theta^D + O(\epsilon^2 De^2), \text{ and} \tag{3.7d}$$

$$\boldsymbol{\tau} = \boldsymbol{\tau}^L + \epsilon De \cdot \boldsymbol{\tau}^D + O(\epsilon^2 De^2). \tag{3.7e}$$

Substituting Eqs. (3.7a - 3.7e) into Eqs. (3.6a - 3.6f) we can gather the leading order terms

$$\frac{\partial u_x^L}{\partial x} + \frac{\partial u_y^L}{\partial y} = 0, \tag{3.8a}$$

$$\frac{\partial \tau_{xx}^L}{\partial x} + \frac{\partial \tau_{xy}^L}{\partial y} + \beta \frac{\partial^2 u_x^L}{\partial y^2} = \frac{\partial p^L}{\partial x}, \tag{3.8b}$$

$$\frac{\partial p^L}{\partial y} = 0, \tag{3.8c}$$

$$\tau_{xx}^L = 0, \tag{3.8d}$$

$$\tau_{xy}^L = -(1-\beta)\frac{\partial u_x^L}{\partial y}, \text{ and} \tag{3.8e}$$

$$\tau_{yy}^L = -2(1-\beta)\frac{\partial u_y^L}{\partial y}. \tag{3.8f}$$

The first order terms are also collected from the substitution and expressed as

$$\frac{\partial}{\partial x}(u_x^D + u_x^L) + \frac{\partial}{\partial y}(u_y^D + u_y^L) \;=\; 0, \tag{3.9a}$$

$$\frac{\partial \tau_{xx}^D}{\partial x} \;+\; \frac{\partial \tau_{xy}^D}{\partial y} \;+\; \beta\frac{\partial^2 u_x^D}{\partial y^2} = \frac{\partial p^D}{\partial x}, \tag{3.9b}$$

$$\frac{\partial p^D}{\partial y} = 0, \tag{3.9c}$$

$$\tau_{xx}^D = 2\frac{\partial u_x^L}{\partial y}\tau_{xy}^L, \tag{3.9d}$$

$$\tau_{xy}^D + \;(1-\beta)\frac{\partial u_x^D}{\partial y} = -\frac{\partial \tau_{xy}^L}{\partial t} - u_x^L\frac{\partial \tau_{xy}^L}{\partial x} \;-\; u_y^L\frac{\partial \tau_{xy}^L}{\partial y} \;+\; \frac{\partial u_x^L}{\partial y}\tau_{yy}^L \;+\; \frac{\partial u_y^L}{\partial x}\tau_{xx}^L, \text{ and} \tag{3.9e}$$

$$\tau_{yy}^D \;+2(1-\beta)\frac{\partial u_y^D}{\partial y} = -\frac{\partial \tau_{yy}^L}{\partial t} - u_x^L\frac{\partial \tau_{yy}^L}{\partial x} \;-\; u_y^L\frac{\partial \tau_{yy}^L}{\partial y} \;+\; 2\frac{\partial u_y^L}{\partial y}\tau_{yy}^L \;+\; 2\frac{\partial u_y^L}{\partial x}\tau_{xy}^L. \tag{3.9f}$$

Note that the linearization of the MPTT constitutive equations gives the same leading and first order terms found in Eqs. (3.8d - 3.8f) and Eqs. (3.9d - 3.9f), respectively. A reference can be made to appendix A for more details.

3.5 Viscoelastic lubricant

We first consider a viscoelastic lubricant where the effects of cavitation are not captured and the fluid is assumed to remain in a single (liquid) phase as has been done by Ahmed and Biancofiore [11]. In a single phase liquid, the fluid fraction term becomes $\theta = 1$, the density everywhere is assumed to be the liquid density ($\rho = \rho_l$).

3.5.1 Pure sliding motion

The typical thin-film flow illustrated in Fig. 3.1 will be considered in this section. The boundary conditions for the pure sliding mode are stated below for the leading order and first order terms as follows

- at $y = 0$: $u_x^L = 1$, $u_y^L = 0$, $u_x^D = 0$ and $u_y^D = 0$
- at $y = h(x)$: $u_x^L = 0$, $u_y^L = 0$, $u_x^D = 0$ and $u_y^D = 0$
- at $x = 0$ and $x = 1$: $p^L = 0$ and $p^D = 0$.

In a pure sliding motion $U_{y,ref} = 0$ and therefore the overall velocity $U_{ref} = U_{x,ref}$.

1. **Zeroth-order solution**
   Solving the leading order terms Eqs. (3.8a - 3.8f) for a lubricant in steady flow we obtain the velocity distribution for the pure sliding motion as

$$u_x^L = \frac{h^2}{2}\frac{\partial p^L}{\partial x}\left(\frac{y^2}{h^2} - \frac{y}{h}\right) + 1 - \frac{y}{h}. \tag{3.10}$$

   Eq. 3.10 can be simplified and solved to derive the zeroth order pressure solution

$$\frac{dp^L}{dx} = 6\frac{h - \alpha}{h^3}, \tag{3.11}$$

   where,

$$\alpha = \frac{\int_0^1 h(x)^{-2}dx}{\int_0^1 h(x)^{-3}dx}. \tag{3.12}$$

   This can be further simplified through integration of Eq. 3.11 and obtaining

$$p^L = 6\int_0^x h^{-2}(s)ds \,-\, 6\alpha\int_0^x h^{-3}(s)ds. \tag{3.13}$$

   The pressure equation for the zeroth order solution (Eq. 3.13) corresponds to the incompressible Reynolds solution derived in chapter 2 for non-cavitating lubricants.

2. **First-order solution**
   Solving the first order governing equations Eqs. 3.9a - 3.9f and applying

the boundary conditions, we are able to arrive at a first order solution for the horizontal velocity

$$u_x^D = \frac{dp^D}{dx}\left(\frac{y^2}{2}-\frac{yh}{2}\right)+\frac{(1-\beta)}{h}\frac{dh}{dx}\left(1-3\frac{\alpha}{h}\right)\left(2-3\frac{\alpha}{h}\right)\left(\frac{y^2}{h^2}-\frac{y}{h}\right), \tag{3.14}$$

To derive the first order pressure solution, Eq. 3.14 is substituted into the first order continuity equation (Eq. 3.9a) to obtain

$$p^D = \frac{9}{2}\left(\frac{\alpha^2}{h^4}-\frac{\alpha^2}{h_0^4}\right)-6\left(\frac{\alpha}{h^3}-\frac{\alpha}{h_0^3}\right)+2\left(\frac{1}{h^2}-\frac{1}{h_0^2}\right)-12h_d\int_0^x \frac{1}{h^3(s)ds}, \tag{3.15}$$

where,

$$h_d = \left[\frac{3}{8}\left(\frac{\alpha^2}{h_1^4}-\frac{\alpha^2}{h_0^4}\right)-\frac{1}{2}\left(\frac{\alpha}{h_1^3}-\frac{\alpha}{h_0^3}\right)+\frac{1}{6}\left(\frac{1}{h_1^2}-\frac{1}{h_0^2}\right)\right]\left(\int_0^1 \frac{1}{h^3(s)}ds\right)^{-1}. \tag{3.16}$$

Note that h_0 and h_1 are the values of $h(x)$ at $x = 0$ and $x = 1$ respectively.

3.5.2 Oscillatory squeeze flow

In this section, we consider the 2-D case of an incompressible, isothermal lubricant between two flat plates. A schematic diagram of the squeeze film case is shown in Fig. 3.2. The bottom plate is kept constant whereas the top plate moves with an oscillatory velocity ($V = dh/dt$) only in the normal direction. The model presented in this section is applicable to flat and curved surfaces, however in this thesis we shall analyze and present results for the former. It is assumed that there is no slippage at the plate boundaries and the ends of the channel maintain a constant atmospheric pressure. The boundary conditions are;

at $y = 0:$ $\quad u_x^L = 0, \quad u_y^L = 0, \quad u_x^D = 0,$ and $\quad u_y^D = 0$

at $y = h(x):$ $\quad u_x^L = 0, \quad u_y^L = 0, \quad u_x^D = 0,$ and $\quad u_y^D = 0$

at $x = 0, 1:$ $\quad p^L = 0,$ and $\quad p^D = 0$

In the squeeze flow configuration we assume that the x-component of the velocity $U_{x,ref} = 0$, this implies that the overall velocity $U = U_{y,ref}$.

1. **Zeroth order solution**

   Solving the leading order governing equations for a single phase fluid and applying the boundary conditions for the oscillatory squeeze problem, a velocity solution is obtained as

$$u_x^L = \frac{1}{2}\frac{\partial p^L}{\partial x}\left(y^2 - yh\right). \tag{3.17}$$

   This velocity equation is simplified and substituted into the continuity equation Eq. (3.8a) (noting that $\theta = 1$) to derive the leading order solution of the Reynolds equation.

$$\frac{\partial p^L}{\partial x} = 12xh^{-3}\frac{dh}{dt} - \alpha_2 h^{-3}, \tag{3.18}$$

   where,

$$\alpha_2 = \frac{12\frac{dh}{dt}\int_0^1 xh^{-3}dx}{\int_0^1 h^{-3}dx}. \tag{3.19}$$

   This solution can be further simplified to arrive at the final form of the zeroth order pressure solution for lubricants in oscillatory squeeze flows

$$p^L = 12\frac{dh}{dt}\int_0^x xh^{-3}dx - \alpha_2\int_0^x h^{-3}dx. \tag{3.20}$$

   This equation corresponds to the Reynolds solution for an incompressible lubricant without introducing the effects of cavitation.

2. **First order solution**

   The first order solution can be found using the De-order terms from the linearized governing equations Eq. (3.9a - 3.9f) and applying the appropriate boundary conditions as stated in section 3.5.2. The velocity equation for the first order oscillatory squeeze flow is

$$u_x^D = \left((1-\beta)\lambda + \frac{1}{2}\frac{dp^D}{dx}\right)\left(y^2 - yh\right), \tag{3.21}$$

   where,

$$\lambda = 36x^2h^{-5}\frac{dh}{dt}^2\frac{dh}{dx} - 6\alpha_2 xh^{-5}\frac{dh}{dt}\frac{dh}{dx} + \frac{\alpha_2^2}{4}h^{-5}\frac{dh}{dx} - 36xh^{-4}\frac{dh}{dt}^2 + 3\alpha_2 h^{-4}\frac{dh}{dt} + 6xh^{-3}\frac{d^2h}{d^2t}\frac{dh}{dx}. \tag{3.22}$$

   A final solution for the first order pressure solution for lubricants is obtained as follows using the continuity equation (Eq. 3.9a)

$$p^D = 12\frac{dh}{dt}\int_0^x xh^{-3}dx - (1-\beta)\int_0^x 2\lambda dx - 12x\frac{dh}{dt}\int_0^1 xh^{-3}dx - (1-\beta)x\int_0^1 2\lambda dx. \tag{3.23}$$

A more accurate solution for a viscoelastic lubricant should include the effects of cavitation in lubricant channels where cavitation is expected to occur. Previous studies have reported negative lubricant pressures where cavitation is expected to occur, implying the lubricant is under tension. Cavitation is known to occur when the tension in a liquid goes beyond a certain critical values known as the cavitation threshold or breaking tension [35]. It has therefore become necessary to improve the viscoelastic lubricant model by introducing a more accurate cavitation model.

3.6 Viscoelastic lubricants with cavitation

In this section we introduce the cavitation problem into the previous formulation for viscoelastic lubricants (see section 3.5). With the presence of cavitation taken into consideration, we now model a multiphase problem where the density ρ can no longer be assumed to be the liquid density ρ_l. Consequently the film fraction θ is no longer taken to be constant ($\theta \neq 1$) at all locations within the lubricant film.

3.6.1 Pure sliding motion

In this section, the typical thin-film flow illustrated in Fig. 3.1 will be reconsidered. The boundary conditions for the pure sliding mode have been stated for the leading order and first order terms in section 3.5.1.

1. **Zeroth order solution**

   The velocity distribution for the pure sliding motion has been obtained as Eq. 3.10. This velocity solution can be simplified and substituted into the compressible continuity equation (Eq. 3.8a) to derive the zeroth order Reynolds solution for lubricant pressure.

   $$\frac{\partial\left(\theta^L u_y^L\right)}{\partial y} = -\frac{\partial}{\partial x}\left[\frac{\theta^L}{2}\frac{\partial p^L}{\partial x}\left(y^2 - yh\right) + \theta^L - \frac{\theta^L}{h}y\right]. \tag{3.24}$$

   This solution can be further simplified through integration by applying the Leibniz rule and obtaining

   $$\frac{\partial}{\partial x}\left(h^3\theta^L\frac{\partial p^L}{\partial x}\right) = 6\frac{\partial(h\theta^L)}{\partial x}. \tag{3.25}$$

   Eq. 3.25 is the proposed zeroth order Reynolds solution taking into account the multiphase property of the fluid. This solution corresponds to the incompressible Reynolds equation for Newtonian fluids when cavitation is present which has been derived in chapter 2.

2. **First order solution**

   The first order solution are a set of linear ordinary differential equations Eqs. (3.9a - 3.9f) which depend on the solution of the zeroth order pressure p^L and fluid fraction θ^L. Solving these equations and applying the boundary conditions, we are able to arrive at a first order solution for the horizontal velocity

$$u_x^D = \frac{dp^D}{dx}\left(\frac{y^2}{2} - \frac{yh}{2}\right) + \frac{(1-\beta)}{h}\frac{dh}{dx}\left(1 - 3\frac{\alpha}{h}\right)\left(2 - 3\frac{\alpha}{h}\right)\left(\frac{y^2}{h^2} - \frac{y}{h}\right). \tag{3.26}$$

To derive the first order Reynolds solution for the lubricant pressure, Eq. 3.10 and Eq. 3.26 are substituted into the first order continuity equation (Eq. 3.9a) and solved using the Leibniz rule obtaining

$$\frac{\partial}{\partial x}\left(h^3\theta^L\frac{\partial p^D}{\partial x}\right) + \frac{\partial}{\partial x}\left(h^3\theta^D\frac{\partial p^L}{\partial x}\right) = 6\frac{\partial(h\theta^D)}{\partial x} - 2(1-\beta)\frac{\partial}{\partial x}\left[\theta^L\frac{dh}{dx}\left(1 - 3\frac{\alpha}{h}\right)\left(2 - 3\frac{\alpha}{h}\right)\right]. \tag{3.27}$$

3.6.2 Oscillatory squeeze flow

In this section, we reconsider the incompressible, isothermal lubricant between two flat plates presented in section 3.5.2 . Recall that the bottom plate remains constant whereas the top plate moves with an oscillatory velocity ($V = dh/dt$) in the normal direction. We assume that there is no slippage at the plate wall boundaries and the ends of the channel maintain a constant atmospheric pressure. The boundary conditions have been stated earlier in section 3.5.2. We also note that the x-component of the velocity $U_{x,ref} = 0$, this implies that the overall velocity $U = U_{y,ref}$.

1. **Zeroth order solution**

   Solving the leading order governing equations and applying the boundary conditions for the oscillatory squeeze problem, a velocity solution has been previously obtained as Eq. 3.17. This equation is simplified and substituted into the continuity equation Eq. 3.8a to derive the leading order solution of the Reynolds equation

$$\frac{\partial\theta^L}{\partial t} + \frac{\partial\theta^L u_y^L}{\partial y} = -\frac{\partial}{\partial x}\left[\frac{\theta^L}{2}\frac{\partial p^L}{\partial x}\left(y^2 - yh\right)\right]. \tag{3.28}$$

Solving this we can arrive at the final form of the zeroth order lubricant pressure solution for oscillatory squeeze flows

$$\frac{\partial}{\partial x}\left(h^3\theta^L\frac{\partial p^L}{\partial x}\right) = 12\frac{\partial h\theta^L}{\partial t}. \tag{3.29}$$

Eq. 3.8 corresponds to the Reynolds solution for an incompressible fluid when cavitation is present.

2. **First order solution**

The first order solution can be obtained using the first order terms from the governing equations Eq. (3.9a - 3.9f) and applying the appropriate boundary conditions as stated in section 3.5.2. The velocity equation for the first order oscillatory squeeze flow has been given as Eq. 3.21. Using this and the compressible continuity equation (Eq. 3.9a) we can obtain a final solution for the first order Reynolds solution for lubricant pressure.

$$\frac{\partial}{\partial x}\left(\frac{h^3}{12}\theta^L\frac{\partial p^D}{\partial x}\right) + \frac{\partial}{\partial x}\left(\frac{\theta^L h^3}{6}(1-\beta)\lambda\right) + \frac{\partial}{\partial x}\left(\frac{h^3}{12}\theta^D\frac{\partial p^L}{\partial x}\right) = \theta^D\frac{\partial h}{\partial t}. \tag{3.30}$$

Eq. 3.27 and Eq. 3.30 are the final forms of the first order Reynolds solution for lubricant pressure in a pure slider bearing and an oscillatory squeeze flow respectively. The zeroth order Reynolds equation is solved as the base case and is implemented towards arriving at solutions for the first order equations. In order to achieve this, it is necessary that a new set of boundary conditions characterizing the full film regions and cavitation boundaries be defined.

3.7 Cavitation boundary condition

The appearance of cavitation in the viscoelastic lubricant will be described using the Elrod-Adams (or p-θ) algorithm [24]. This algorithm was reported to be much more accurate for squeezing problems and the sliding micro-textured profile when compared to other models using the half-Sommerfeld condition in predicting the lubricant behavior [2, 28].

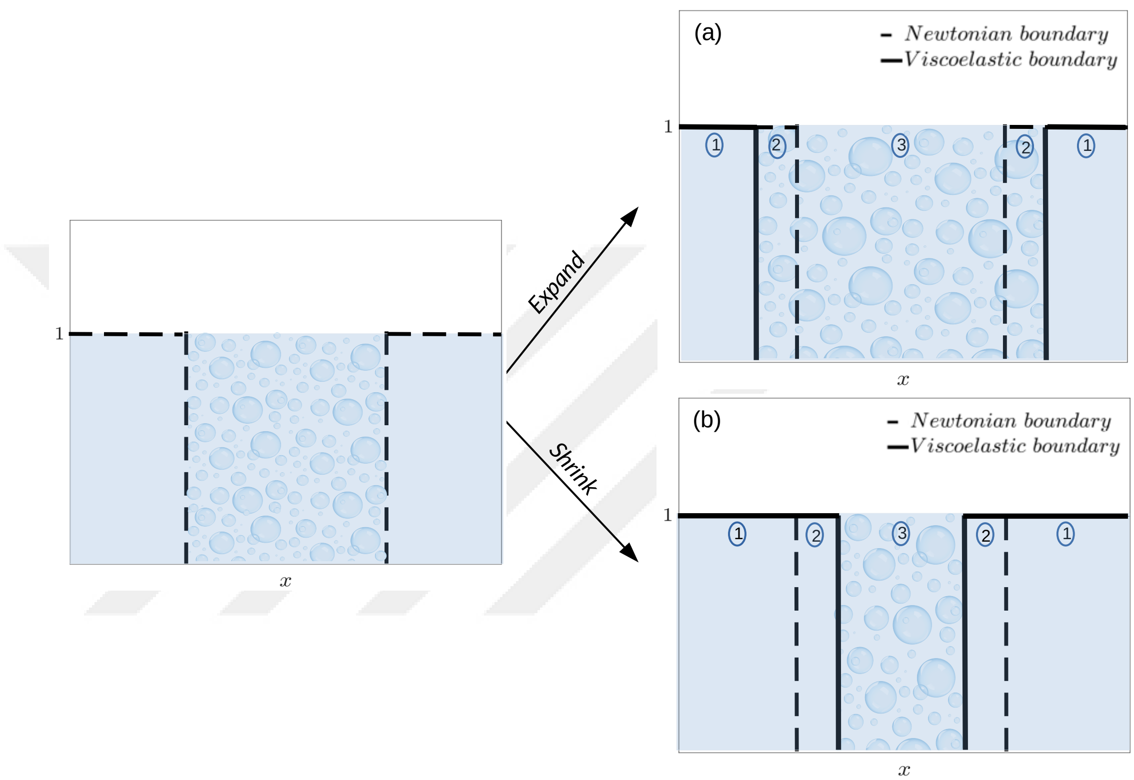

Figure 3.3: Transition of the non-active region location from Newtonian to viscoelastic lubricant when the cavitation region is (a) extended and (b) shrinked by adding polymers to the fluid.

We assume that the pressure remains constant in the non-active region and equal to the cavitation pressure $p = p_{cav}$. Then the pressure gradient is zero ($\frac{dp}{dx} = 0$). In the cavitation region, it is convenient to use the fluid fraction θ as the dependent variable rather than the pressure. This fluid fraction term can be regarded as an auxiliary quantity used to determine the appropriate conditions to apply at both the incompressible liquid region and the compressible vapor-liquid mixture region

$$\theta = \begin{cases} 1, & \text{in the incompressible full-film region,} \\ 0 < \theta < 1, & \text{in the compressible mixture region.} \end{cases} \tag{3.31}$$

Viscoelasticity has an effect on both the location of film rupture and reformation. Therefore it is necessary to define a new set of boundary conditions which are capable of accurately capturing the changes as a result of the perturbation expansion when transitioning from Newtonian to non-Newtonian for the active and non-active regions within the viscoelastic lubricant. An illustrative description of the boundaries can be seen in Fig. 3.3. The region labeled as 1 is liquid for both Newtonian and viscoelastic cases, while in the region labeled 2 a phase transition (either from liquid to mixture or from mixture to liquid) occurs between the Newtonian and the viscoelastic lubricant cases. Finally the region labeled 3 contains some vapor for both Newtonian and viscoelastic films. Two cases are possible:

1. If the cavitation region expands as a result of increasing viscoelastic effects in the lubricant, some parts of the contact initially occupied purely by a full-film ($\theta = 1$) in the Newtonian case undergo a phase transition. For this reason we have a liquid-vapor mixture ($\theta < 1$). Fig. 3.3a shows a schematic of an increasing cavitation region due to the lubricant viscoelasticity

   - $p^D = \frac{-p^L}{\epsilon De}$ in the two regions in which a mixture is present for the viscoelastic case (2 and 3).
   - $\theta^D = \frac{1-\theta^L}{\epsilon De}$ in the unchanged full-film region 1.
   - $p^L = 0$ in region 3 where the fluid is a mixture in both the Newtonian and the viscoelastic cases.

2. The reverse case is expected for a shrinking cavitation region, i.e. when mixture regions for the Newtonian case are occupied by liquid if the film is viscoelastic. Fig. 3.3c shows a schematic of a shrinking non-active region as a result of increasing viscoelastic effects.

   - $p^D = \frac{-p^L}{\epsilon De}$ in the unchanged mixture region 3.
   - $\theta^D = \frac{1-\theta^L}{\epsilon De}$ in the two regions (i.e. 1 and 2) fully occupied by liquid if the film is viscoelastic.
   - $\theta^L = 1$ in region 1, i.e. the region in which we have liquid independently if it is Newtonian or viscoelastic.

Finally, the cavitation boundary for the squeeze flow problem is transient ($\frac{\partial\theta}{\partial t} \neq 0$), resulting in different phases at the same location over a time period.

Although we derived two sets of equations for the zeroth order and the first order lubricant pressure, four unknowns (p^L, p^D, θ^L and θ^D) still remain. Using the Elrod-Adams model, we are able to obtain a solution at all nodes. This solution is achievable as only one variable in the equations is unknown in each region. For instance in the full-film region the fluid fraction is known ($\theta = 1$) while in the non-active region the pressure is known ($p = p_c$).

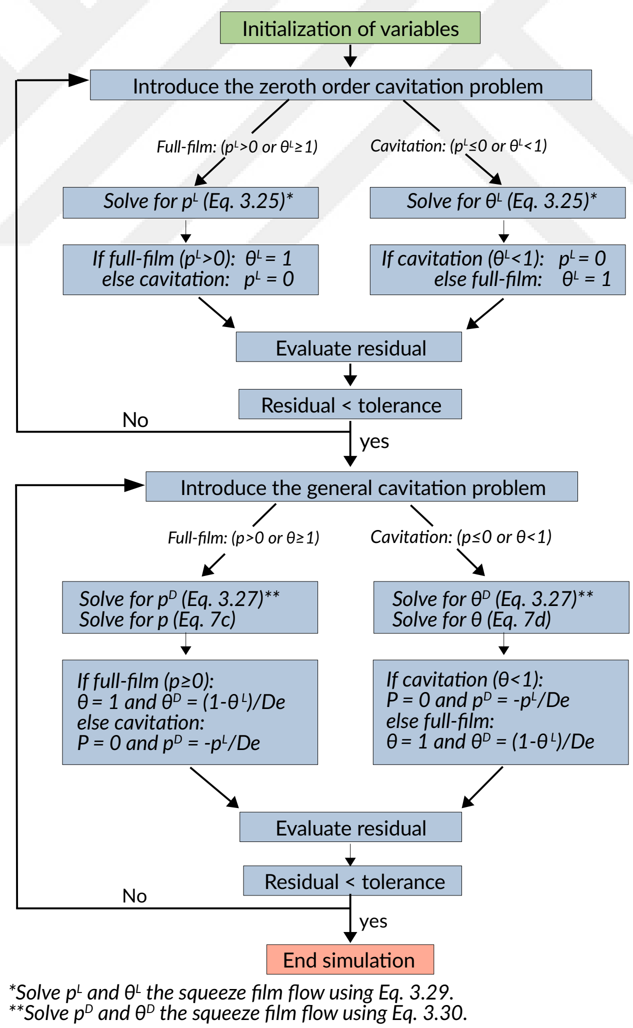

Figure 3.4: The flow chart of the viscoelastic Elrod-Adams algorithm used in the present study.

3.8 Numerical method and algorithm

Solutions to the zeroth order and first order pressures (p^L and $\mathrm{p^D}$) derived for both the pure sliding and squeeze film flow configurations in a single phase viscoelastic lubricant have been presented in sections 3.5.1 and 3.5.2 respectively. These can now be solved directly by the numerical integration of the corresponding pressure terms. To solve the Reynolds equation for cavitating lubricants, we consider Ausas and co-authors who have presented in their work an efficient Elrod-Adams algorithm using a finite difference numerical scheme [28, 2]. Their numerical algorithm has been modified to incorporate the newly defined set of boundary conditions (see section 3.7 and the constitutive equations to model viscoelastic lubricants.

A flow chart of the algorithm used in this study is shown in Fig. 3.4. Firstly, we solve the zeroth order problem (Eq. 3.25 and Eq. 3.29 for the slider and squeeze flow, respectively) since p^L and θ^L are both needed to solve the first order equations (Eq. 3.27 and Eq. 3.30 for the slider and squeeze flow, respectively). Afterwards we solve the general linearized set of equations. We employed a finite difference numerical scheme by approximating the spatial derivative for the shear flow term using the backward differencing scheme. The backward differencing scheme is important in the cavitation region where the equation becomes hyperbolic and no data is coming from the down-stream region [27]. The pressure induced flow term has been approximated using the discrete equation

$$\frac{\partial}{\partial x}\left(h^3\theta\frac{dp}{dx}\right) = \frac{1}{\Delta x^2}\left[h_i^3\theta_i(p_{i+1}-p_i) - h_{i-1}^3\theta_{i-1}(p_i - p_{i-1})\right], \tag{3.32}$$

and is applicable to both leading order and first order terms. The transient term had been discretized with the Euler backward scheme, which numerically is a very stable method. We choose as number of grid points N = 400 to ensure grid independence for both the journal bearing and the oscillatory squeeze flows. For the surface textured profiles, we chose a larger number of grid points (N = 1000) in order to adequately capture the film behavior at the edges of the pocket. A time step equal to $\Delta t = 6.6{*}10^{-4}$ was found suitable for the transient simulations. Convergence at nodal point i for time step j of the s^{th} iteration was reached when

$$||p^s_{i,j} - p^{s-1}_{i,j}||_2 + ||\theta^s_{i,j} - \theta^{s-1}_{i,j-1}||_2 \leq tolerance, \tag{3.33}$$

where a tolerance of 10^{-6} was set for all simulations. For the steady state solutions, we use the same equation to calculate the error convergence but ignore the transient terms. A Gauss-Seidel iteration scheme was employed in determining the solution convergence.

Chapter 4

Numerical solution and results

In this chapter, several bearing configurations are examined, particularly, analysis are conducted for the pure sliding and oscillatory squeeze film flow using (i) the parabolic profile geometry configuration representing an unwrapped journal bearing, (ii) single and multi-pocketed slider configurations representing a surface texture, and (iii) the oscillating squeeze motion of lubricants held between two parallel plates. Analysis will be carried out for all three configurations in a single phase lubricant (i.e no cavitation) in section 4.1 and will be extended to presenting results when cavitation is present in section 4.2. The results of the Newtonian lubricant when cavitation is present are validated in section 4.2.1 by comparing with earlier works of Giacopini et al. [1] for the roller bearing and Ausas et al. [2] for the oscillatory squeeze flow.

4.1 Viscoelastic lubricants

In this section, different profile configurations for the single phase lubricants are examined. We begin by conducting an analysis on an unwrapped journal bearing represented by a cosine profile configuration in section 4.1.1. A surface textured bearing is modeled using a pocketed slider configuration in section 4.1.2, and finally the oscillatory squeeze film flow of a lubricant is considered in section 4.1.3.

4.1.1 Journal bearing

The unwrapped journal bearing is modeled using the cosine profile shown in Fig. 4.1. The top surface of the cosine slider remains constant and the bottom surface moves with a constant sliding velocity as indicated by the red arrow. This profile has been defined using

$$h(x) = c\left[1 + \frac{\varepsilon}{c} cos\left(\frac{2\pi k x}{a}\right)\right], \tag{4.1}$$

where the eccentricity ε is $\varepsilon = 0.2$, the clearance c is $c = 0.8$, the spatial frequency k is $k = 1$, and the non-dimensional atmospheric pressure p_a is $p_a = 0.0083$. An atmospheric boundary condition is imposed at the inlet and outlet boundaries ($p(0) = p(1) = p_a$).

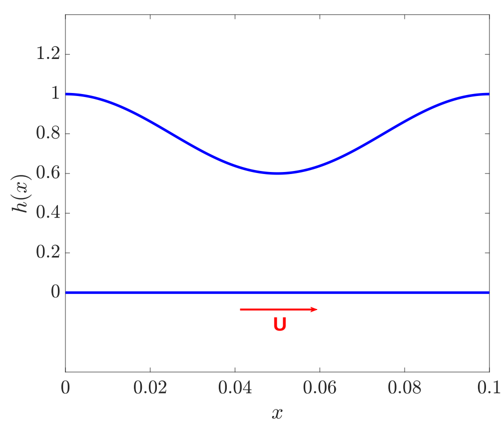

Figure 4.1: The cosine profile mimicking an unwrapped journal bearing.

The pressure distribution in the cosine slider for a single phase viscoelastic lubricant is shown in Fig. 4.2a. It can be noted that the maximum pressure of the lubricant increases with increasing viscoelastic effects. The first order pressure contribution has been reported in Fig. 4.2b. Increasing viscoelastic effects leads to a larger first order pressure contribution within the lubricant.

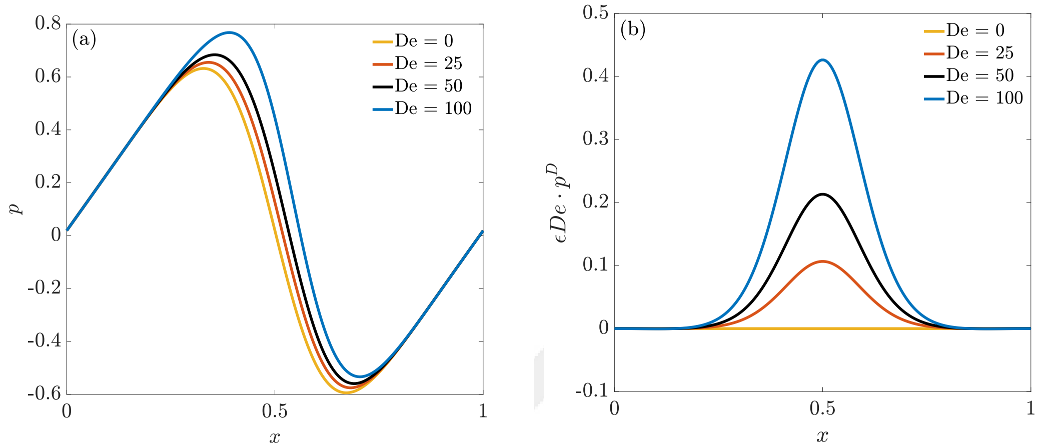

Figure 4.2: Single phase lubricant (a) pressure distribution p in the cosine slider at various Deborah numbers and (b) first order pressure p^D in the cosine slider at several values of the Deborah number: $De = 0$ (yellow lines), $De = 25$ (red lines), $De = 50$ (black lines) and $De = 100$ (blue lines).

4.1.2 Surface texture

Surface textures have been introduced in lubricated contacts because of their potential to improve the performance of the mechanical components, particularly to reduce friction [36].

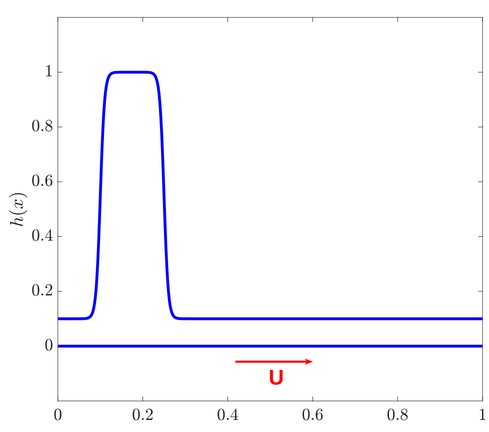

Figure 4.3: Pocket profile geometry modeling a surface texture.

We model a textured bearing using the pocketed profile shown in Fig. 4.3. The surface geometry is characterized by the equation

$$h(x) = h_{min} + \frac{1 - h_{min}}{2 * tanh(100 * (x - b))} - \frac{1 - h_{min}}{2 * tanh(100 * (x - b - c))}, \quad (4.2)$$

where the entrance height h_{min} is $h_{min} = 0.1$, the non-dimensional atmospheric pressure p_a is $p_a = 0.05$, the pocket length c is $c = 0.15$ and the entrance length b is $b = 0.1$. This profile is inspired from the pocket profile used by Biancofiore et al. [37], but slightly modified to smoothen the pocket edges to avoid that the discontinuities associated with textured surfaces that lead to numerical instabilities in the polymer constitutive equation.

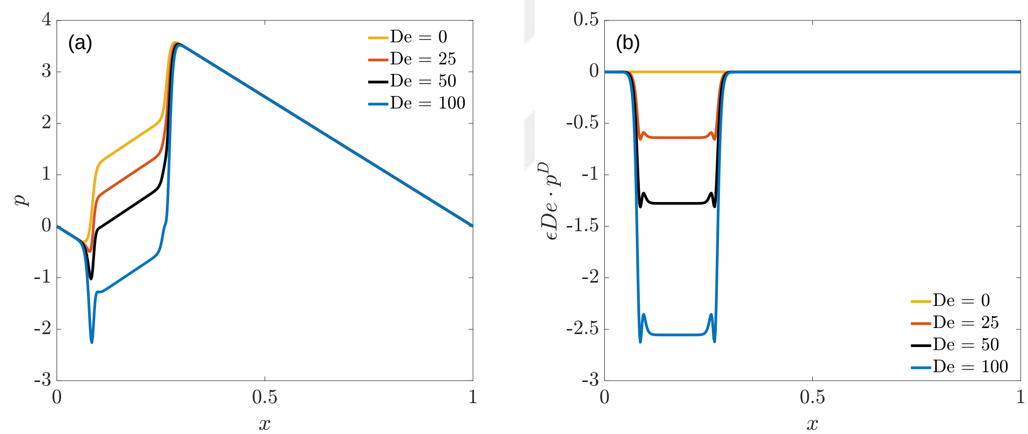

Figure 4.4: Single phase lubricant (a) pressure distribution p in the pocket slider at various Deborah numbers and (b) first order pressure p^D in the pocket slider at several values of the Deborah number: $De = 0$ (yellow lines), $De = 25$ (red lines), $De = 50$ (black lines) and $De = 100$ (blue lines).

Analysis for a single phase viscoelastic lubricant in a surface textured profile has been carried out and Fig. 4.4a is the pressure distribution within the pocket pad. The results indicate that there is a decrease in the minimum pressure with increasing viscoelastic effects. This is also observable in the first order pressure results shown in Fig. 4.4b where larger viscoelastic effects corresponds to a lower first order pressure contribution. An increase in the region with negative pressures with increasing viscoelastic effects means stronger cavitation effects are to be expected. To confirm this, we need to consider the results from our model which analyzes the presence of cavitation in viscoelastic lubricant films.

4.1.3 Oscillatory squeeze flow

In this section, we consider the oscillatory squeeze flow between two rigid flat plates as described in Fig. 3.2. The bottom plate is kept constant and the top plate moves only in the vertical direction. The top surface profile is described by the spatial and time dependent function

$$h(x,t) = h_0 + h_1 cos(\omega t) + ax^2, \tag{4.3}$$

where h_0 is the clearance height, h_1 is the amplitude of motion, ω is the oscillation frequency, a is a factor of curvature for the moving plate and the reference velocity

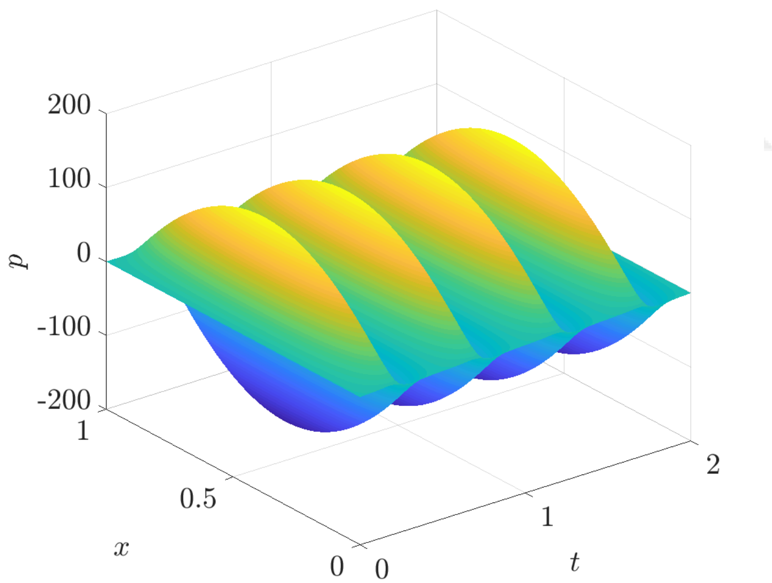

Figure 4.5: Lubricant pressure distribution p in the oscillatory squeeze film flow at all points within the channel over a time period t.

$V_{ref} = \omega h_1$. We set $h_0 = 0.375$, $h_1 = 0.125$, $\omega = 4\pi$ and $a = 0$ to represent two flat and parallel plates. This flat profile is common in modeling squeeze films and has been used in a finite element analysis of the Newtonian squeeze flow problem by Optasanu et al. [38]. At the boundaries, the pressure is set to atmospheric pressure, $p_a = 0.1358$.

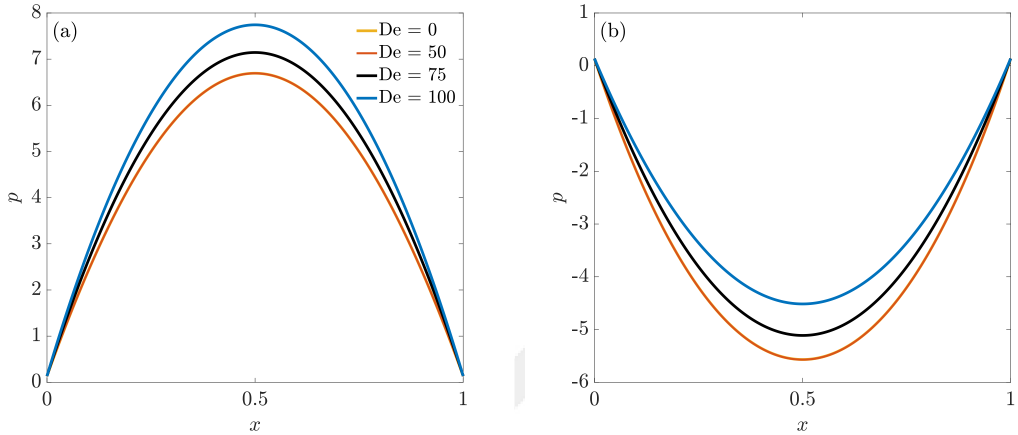

Figure 4.6: Single phase lubricant pressure distribution p in the oscillatory squeeze film flow when (a) t = 0.25 and (b) t = 0.7 for several values of the Deborah number: $De = 0$ (yellow lines), $De = 25$ (red lines), $De = 50$ (black lines) and $De = 100$ (blue lines).

The pressure profile for a single phase lubricant highlighting both the positive and negative squeeze motions is shown in Fig. 4.6. At time $t = 0.25$ during which the plates are being brought together the compression force leads to a positive pressure whose magnitude increases with increasing viscoelastic effects as shown in Fig. 4.6a. On the other hand, when the plates undergo negative squeezing (separation), the lubricant has negative pressures (see Fig. 4.6b). The negative pressure regime indicates that this is an insufficient viscoelastic model as the effects of cavitation are not well captured. This necessitates an improvement towards a better model that captures and defines more accurately the presence and effect of cavitation. To do so, we consider and solve the model for viscoelastic lubricants when cavitation is present.

4.2 Viscoelastic lubricants with cavitation present

In this section, we examine several profile configurations for a pure sliding and oscillatory squeeze film flow of viscoelastic lubricants when cavitation is present. The section begins by validating results of our Newtonian case with the works of Giacopini et al. [1] for pure sliding cases and Ausas et al. [2] for the oscillatory squeeze flow case in section 4.2.1. This will be followed by an analysis conducted on a (i) parabolic profile geometry to represent an unwrapped journal bearing configuration in section 4.2.2 and (ii) single and multi-pocket slider configurations to model a surface texture in section 4.2.3. Finally, an analysis of the oscillatory squeeze motion of two parallel plates is carried out and results presented in section 4.2.4.

4.2.1 Validation

The proposed model is validated by comparing our model when $De = 0$ (the leading order solution) and other Newtonian cases in literature. The Newtonian solution is also achievable by setting the solvent concentration $\beta = 1$. We validate our results for the pure sliding case, by comparing with results obtained by Giacopini et al. [1]. The cosine profile shown in Fig. 4.1 was used to mimic an unwrapped journal bearing geometry with the film thickness defined by Eq. 4.1. The reader is referred to section 4.1.1 for the geometry properties used for the cosine profile in this validation. This configuration is commonly used to test

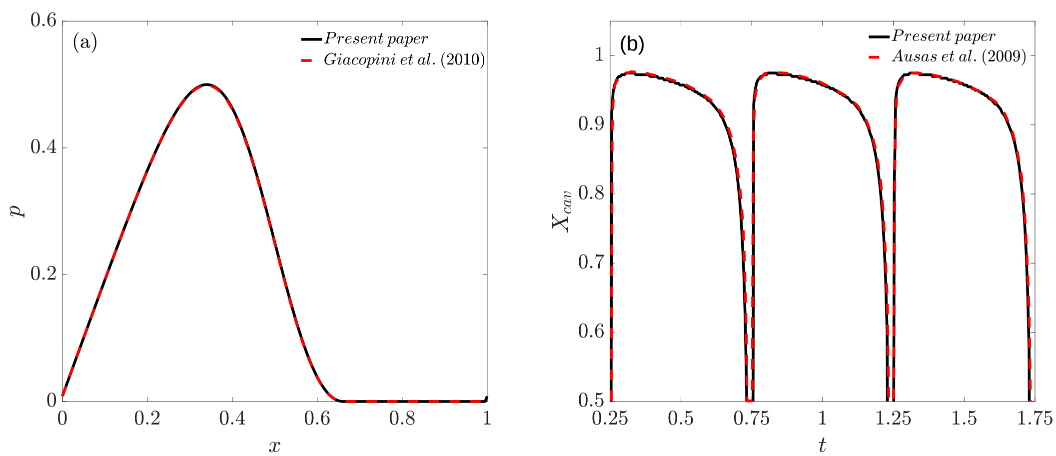

Figure 4.7: Validation of the film pressure for a Newtonian case in (a) a cosine slider bearing, and (b) a squeeze film flow. The black continuous lines illustrate the results obtained by our algorithm whereas the red dashed lines are (a) results of Giacopini et al. [1] and (b) results of Ausas et al [2], respectively.

algorithms describing cavitation appearance in lubrication, see e.g. Biancofiore et al. [37] who studied the effects of slippage at the walls of lubricated contacts in the presence of cavitation.

The lubricant pressure distribution for the current configuration is shown in Fig. 4.7a. The dashed lines are the values obtained by Giacopini et al. [1], whereas the continuous lines indicate our results. We are satisfied by the predictions of our model, since the two curves are identical. We validate our algorithm for the oscillatory squeeze flow between two rigid flat plates by comparing to the mass-conserving algorithm proposed by Ausas et al. [2]. The bottom plate is kept constant and the top plate moves only in the vertical direction. The top surface profile is described by the spatial and time dependent function given in Eq. 4.3 with the exact configuration used in section 4.1.3 to be used here. Note that the proposed algorithm can be easily extended to other curved configurations. We impose (i) an initial full-film condition $\theta(x, t = 0) = 1$, and (ii) a full-film boundary condition at $\theta(0, t) = \theta(1, t) = 1$. At the boundaries, the pressure is set to $p_a = 0.1358$ for both Newtonian and viscoelastic solutions.

Fig. 4.7b shows the position of the right cavitation boundary $X_{cav}(t)$. The dashed line are the values obtained by Ausas et al. [2], whereas the continuous line represents the position of the boundary determined by the proposed model. We conclude that our algorithm is able to reproduce correctly the results found in literature when the film is Newtonian.

4.2.2 Journal bearing

In this section, we investigate the effects of viscoelasticity in lubricant films by utilizing two profiles representing an unwrapped geometry of a journal bearing. Particularly, in section 4.2.2.1 we analyze the parabolic profile already used by Sahlin et al. [27] and Vijayraghavan et al. [31], whereas in section 4.2.2.2 we focus on a twin parabolic slider used by Bertocchi et al. [39]. In section 4.2.2.3 we briefly examine the effect of the solvent concentration on the bearing performance. Finally, we analyze in section 4.2.2.4 the effect of viscoelasticity on the load carrying capacity of both profiles.

4.2.2.1 Parabolic profile

The parabolic profile, which is illustrated in Fig. 4.8 has been shown to induce cavitation at the diverging end of the channel. The top surface of the parabolic slider does not move and the bottom surface has a constant sliding velocity. The parabolic profile is defined by

$$h(x) = h_{min}\left[1 + \frac{(x-0.5)^2}{0.25}\right]. \tag{4.4}$$

In this configuration the minimum film height h_{min} is $h_{min} = 0.5$. The boundary condition imposed at the inlet and outlet of the channel is $p_a = 0.019$ and the corresponding fluid fraction at these boundaries is set to $\theta = 1$.

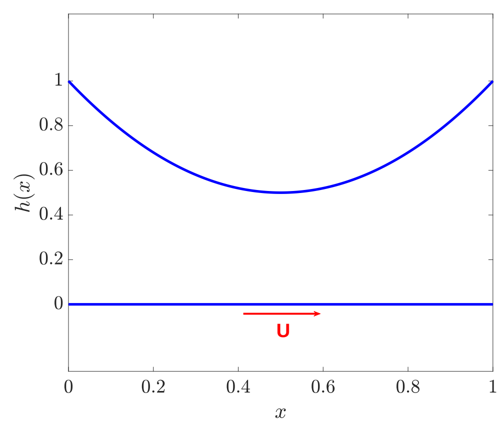

Figure 4.8: The unwrapped journal bearing modeled as a parabolic profile.

Fig. 4.9a shows the pressure distribution in the parabolic slider for viscoelastic lubricants using the proposed algorithm. One can note that the maximum pressure within the channel increases when viscoelastic effects become stronger as will be shown in Table 4.1. Fig. 4.9b is the first order pressure contribution in the parabolic slider. An increase in p^D is a measure of the viscoelastic contribution to modify the pressure. Film fraction results in Fig. 4.9c shows the incompressible liquid region where $\theta = 1$ and the compressible mixture region where $\theta < 1$. Fig. 4.9c indicates that there is a change in the film rupture location as viscoelastic

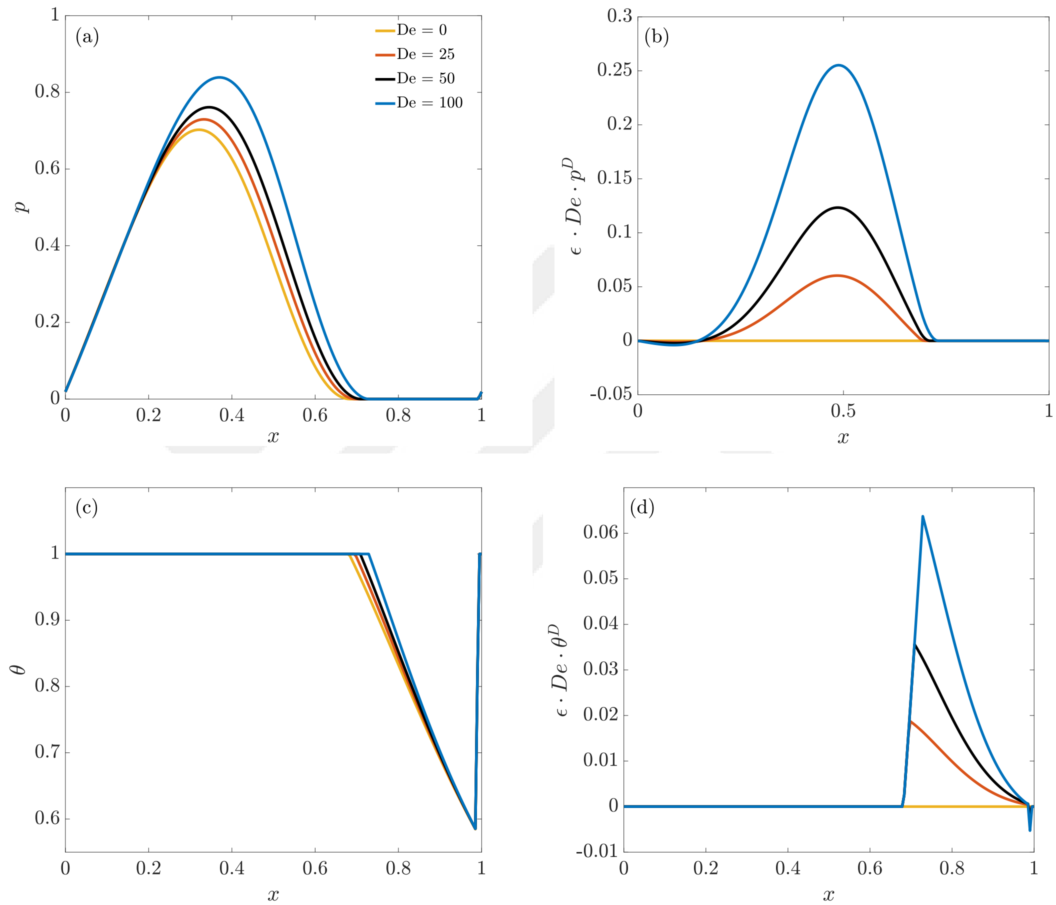

Figure 4.9: (a) Pressure distribution p in the parabolic slider at various Deborah numbers, (b) the first order pressure p^D in the parabolic slider at various Deborah numbers, (c) film fraction θ at several values of the Deborah number and (d) the first order film fraction θ^D at several values of the Deborah number: $De = 0$ (yellow lines), $De = 25$ (red lines), $De = 50$ (black lines) and $De = 100$ (blue lines).

effects become stronger (De increases). The location of the cavitation boundary moves towards the outlet if polymers are added to the lubricant, whereas the reformation boundary remains constant. This suggests a reduction of the entire cavitation region with increasing De as confirmed in Table 4.1. Fig. 4.9d shows the first order film fraction, where a positive value of θ^D implies that the cavitation region shrinks and vice versa. Positive values for the first order film fraction within the cavitation region indicates there is an increase in the overall film fraction towards a full film. The spike close to the reformation location is an exaggerated effect resulting from a sharp change in the film fraction. Since we have assumed no viscoelastic effects in the cavitation region, the spike accounts for the sudden change in the film fraction at that location.

Deborah number	Maximum pressure	% of cavitated region
0	3.73 MPa	30.64
25	3.87 MPa	29.13
50	4.04 MPa	28.14
75	4.23 MPa	26.63
100	4.45 MPa	26.13

Table 4.1: Lubricant maximum pressure and extent of cavitation region data for a parabolic slider at various Deborah numbers.

4.2.2.2 Twin parabolic profile

To verify the accuracy of the proposed algorithm in handling the lubricant film reformation, we investigate the flow in a twin parabolic slider represented in

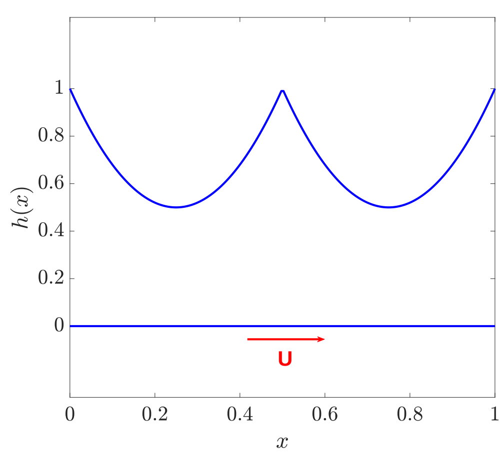

Figure 4.10: The unwrapped journal bearing modeled as a twin parabolic profile.

Fig. 4.10. This peculiar profile has two separated non-active regions. In particular, for the first parabolic region, reformation occurs far away from the outlet [39]. This allows to have a better understanding of the influence polymer additives have on the reformation location. The twin parabolic slider is represented by

$$h(x) = h_{min} + 16 \cdot h_{min} \begin{cases} \left(x - \frac{1}{4}\right)^2, & 0 \leq x \leq \frac{1}{2}, \\ \\ \left(x - \frac{3}{4}\right)^2, & \frac{1}{2} \leq x \leq 1, \\ \end{cases} \tag{4.5}$$

where $h_{min} = 0.5$. The boundary condition imposed at the inlet and outlet of the channel is $p_a = 0.019$ with fluid fraction at these boundaries set to $\theta = 1$.

The pressure distribution for different values of De is shown in Fig. 4.11a. An increase in the maximum pressure is observed as viscoelastic effects are introduced and made stronger, similar to the parabolic slider in section 4.2.2.1. Fig. 4.11b shows an increase in the first order pressure as viscoelastic effects grow, similar to what has been reported in section 4.2.2.1. The film fraction for the twin parabolic slider in Fig. 4.11c shows two regions of cavitation as expected. Furthermore, we observe a reduction in the cavitation region as De becomes larger. However, there is no significant effect of viscoelasticity on the reformation boundary of the twin parabolic slider. The effect of viscoelasticity on these regions is emphasized by Fig. 4.11d where a positive θ^D suggests that the non-active region becomes smaller if the viscoelastic effects get stronger in the lubricant. The spikes are also observed here as a result of the reported increase in the film fraction within the cavitation region and the sudden transition from a non-active to active region at the reformation location.

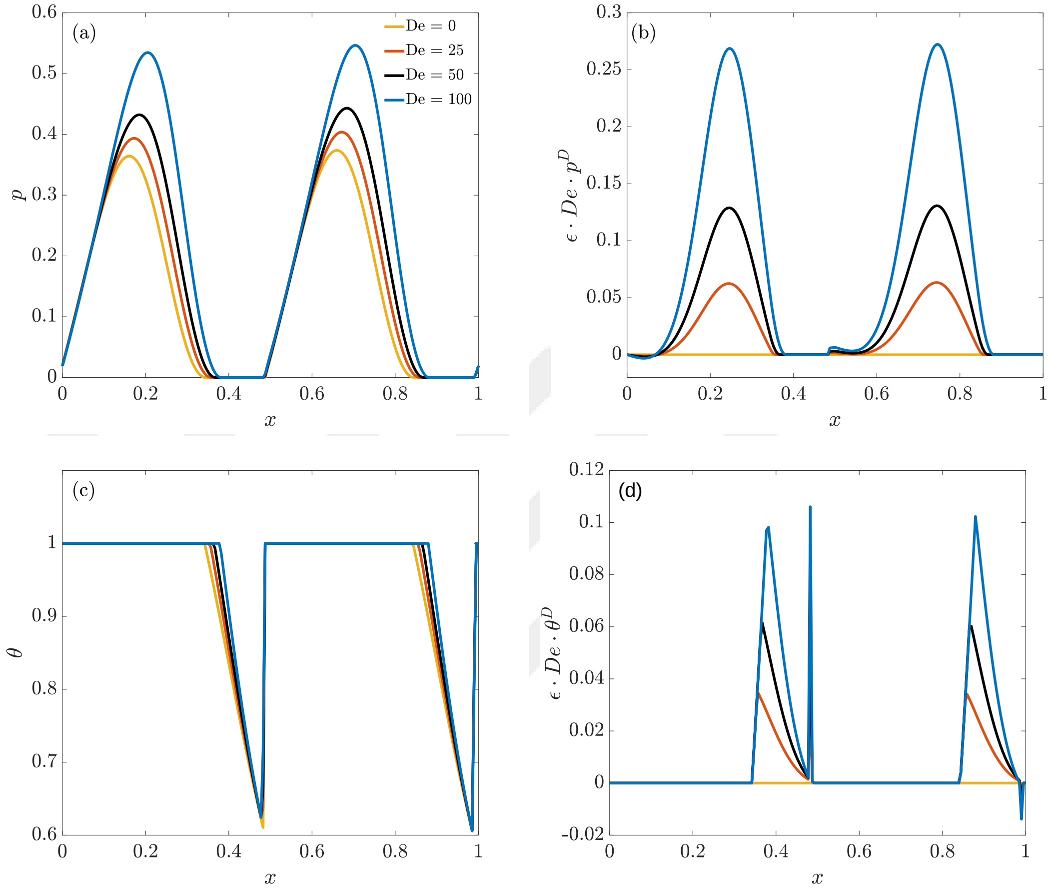

Figure 4.11: (a) Pressure distribution p in the twin parabolic slider, (b) the first order pressure p^D in the twin parabolic slider, (c) the film fraction θ distribution in the twin parabolic slider, and (d) the first order film fraction θ^D in the twin parabolic slider, for various Deborah numbers: $De = 0$ (yellow lines), $De = 25$ (red lines), $De = 50$ (black lines) and $De = 100$ (blue lines).

4.2.2.3 Effect of solvent concentration on lubricant pressure

We analyze the effect of solvent concentration on the film pressure. Fig. 4.12a and Fig. 4.12b show the pressure distributions for various solvent concentrations at $De = 50$ in the parabolic slider and twin parabolic slider configurations, respectively. By decreasing the polymer concentration $(1 - \beta)$, the viscoelastic properties of the fluid become weaker. This results in a gradual return to the Newtonian solution which is achieved when the solvent concentration is maximum $(\beta = 1)$. We can conclude that a decrease in β is equivalent to an increase

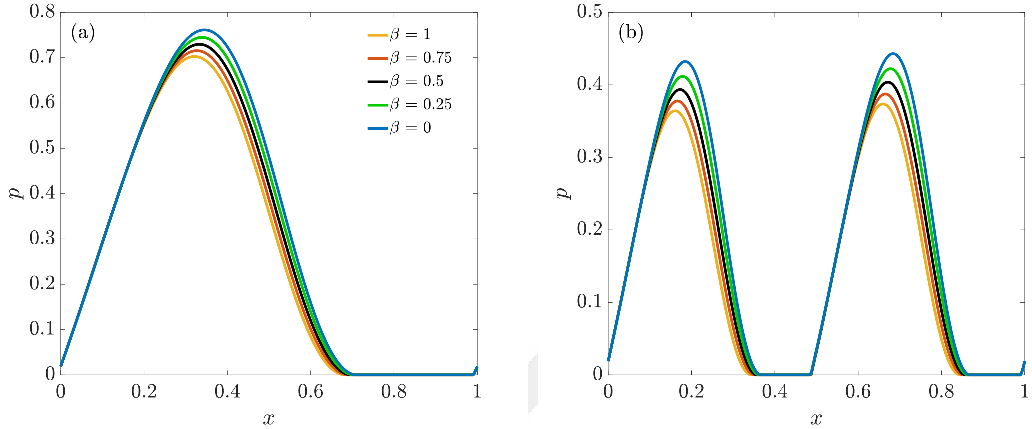

Figure 4.12: The lubricant pressure in (a) the parabolic slider, and (b) the twin parabolic slider, for $De = 50$ and different values of the solvent concentration: $\beta = 1$ (yellow lines), $\beta = 0.75$ (red lines), $\beta = 0.5$ (black lines), $\beta = 0.25$ (green lines) and $\beta = 0$ (blue lines).

in De. Then a steady rise in the film pressure occurs as the viscoelastic effects (i.e. either an increase of relaxation time or an increase of polymer concentration) become stronger.

4.2.2.4 Effect of viscoelasticity on journal bearing load

In this section we study how viscoelasticity influences the load carrying capacity of lubricants. The total load W is calculated as

$$W = \int p(x)dx = \int \left(p^L(x) + \epsilon De \cdot p^D(x)\right) dx. \tag{4.6}$$

Moreover we define W_0 to be the load for the Newtonian case. Fig. 4.13 shows the load within the parabolic profile and twin parabolic profile as a function of the Deborah number. As expected the load carrying capacity increases linearly for both profiles confirming the beneficial influence of the polymer additives for lubricants in journal bearings.

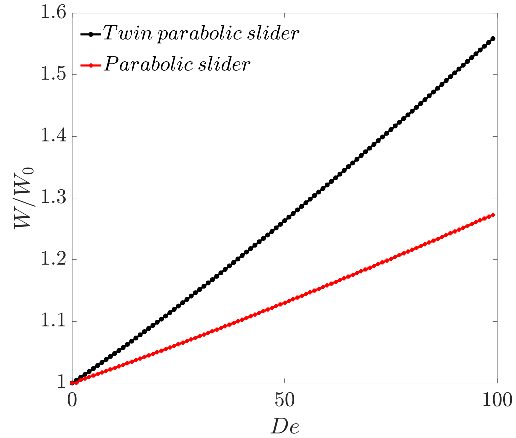

Figure 4.13: Normalized load for a parabolic slider (red line) and a twin parabolic slider (black line) in function of the Deborah number.

4.2.3 Surface texture

In this section we study the impact of viscoelastic lubricants with cavitation present on surface textured contacts. Particularly, we analyze the influence of the location of the texture. We model a textured bearing using the pocketed

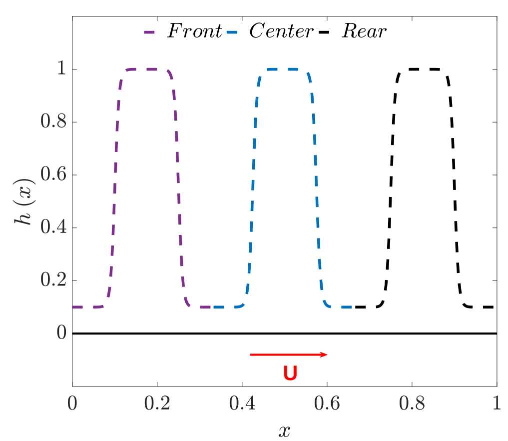

Figure 4.14: A surface textured bearing modeled using three pockets at the front, center and rear sections of the channel.

profile shown in Fig. 4.14. The surface geometry is characterized by Eq. 4.2 which has been used earlier in section 4.1.2. We recall that the entrance height

h_{min} is $h_{min} = 0.1$, the non-dimensional atmospheric pressure p_a is $p_a = 0.05$, the pocket length c is $c = 0.15$ and the entrance length b is (i) $b = 0.1$ at the front pocket, (ii) $b = 0.425$ at the center pocket and (iii) $b = 0.75$ at the rear pocket.

An analysis using the proposed algorithm for the textured surface with the pocket located at (i) the front, (ii) center, (iii) rear of the channel, and (iv) a multi-pocket, i.e. a combined profile including all the pockets, has been carried out. Fig. 4.15 shows the pressure distribution at different pocket locations at several values of the Deborah number. For all the configurations the maximum pressure is observed to first decrease and eventually increases as Deborah number becomes larger. However the degree of the increase of the pressure varies significantly with the position of the pocket. If the pocket is located close to the entry (see Fig. 4.15a) the value of the maximal pressure at high De is still lower than the Newtonian case, for all the other geometries the maximum maximorum for the pressure is for $De = 50$ between the analyzed values. Particularly the highest increase of pressure at high De is observed when the pocket is located close to the exit (see Fig. 4.15c). The pressure profile of the multi-pocket configuration (see Fig. 4.15d) shows multiple cavitation and reformation locations in the film.

Interestingly, one can note that the pressure before (after) the cavitated region grows (decreases) as polymers are added to the lubricant pointing how the sign of dh/dx plays a role in defining the influence of viscoelasticity [40]. Also the size of the non-active region is influenced by the polymer addition. Particularly the reformation position is strongly affected by the polymers since the decrease in pressure can bring to an extension of the cavitation region.

Fig. 4.16a compares the load for different configurations at various values of the Deborah number. For a single pocket located at the front section of the channel, there is an initial decrease in load as De increases. This trend is reversed and a small but steady increase in load is observed beyond $De = 20$. The decrease in load observed at low values of the Deborah number can be attributed to the pressure decrease and the consequent retardation of the film reformation. However, the increase of the pressure, observed before the cavitation sections, results eventually in a load enhancement once it is able to balance the pressure

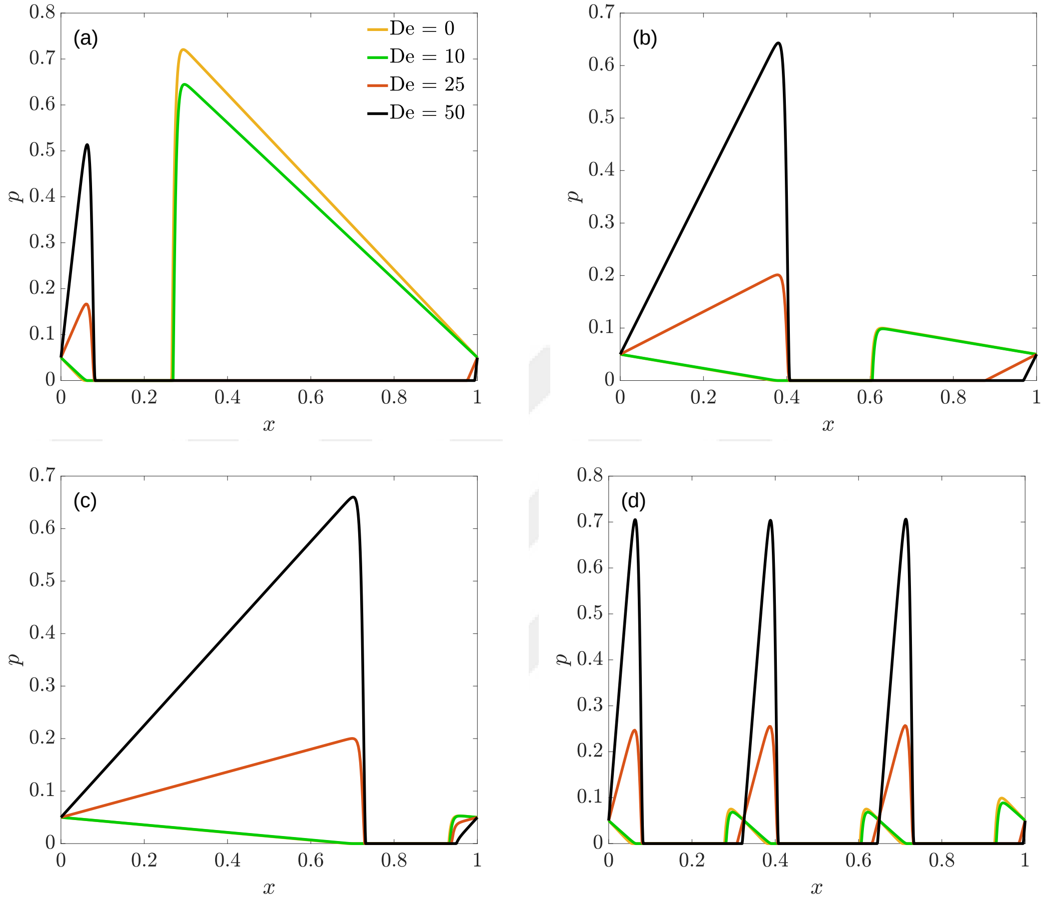

Figure 4.15: The lubricant pressure distribution p in the pocketed slider with the texture located at the (a) front (b) middle (c) rear location and in (d) multiple positions for $De = 0$ (yellow lines), $De = 10$ (green lines), $De = 25$ (red lines) and $De = 50$ (black lines).

decrease occurring at the film reformation. For the center and rear pockets, the load remains almost constant at lower values of the Deborah number as the two opposite effects previously described balance each other. At larger values of De the contribution of the rising pressure dominates causing the increase in the load carrying capacity. Finally, the friction is calculated as

$$F = \int_0^1 \tau_{xy}\, dx = \int_0^1 \left(\frac{\partial u^L}{\partial y} + \epsilon De \frac{\partial u^D}{\partial y} \right) dx. \tag{4.7}$$

We define as F_0 the value of the friction for $De = 0$. The friction comparison in

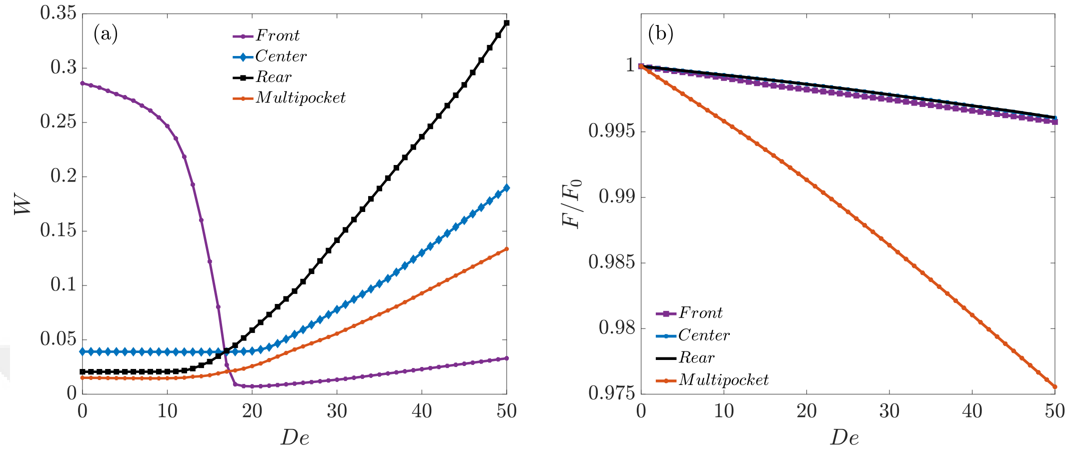

Figure 4.16: (a) Load and (b) normalized friction comparisons at different Deborah numbers for the four different surface textured configurations.

Fig. 4.16b shows the normalized friction (F/F_0) at different values of the Deborah number. One can note that the viscoelasticity slightly reduces the friction in the pocketed bearing. This effect is negligible but it is important to note that polymer additives do not create additional friction. This points out how these additives could be suitable for usage also in surface textured contacts.

4.2.4 Oscillating squeeze film

The oscillatory squeeze flow of viscoelastic lubricants between two rigid parallel plates shown in Fig. 3.2 will be analyzed in this section. The bottom plate is kept constant and the top plate moves only in the vertical direction. The temporal evolution of the top surface is the same used in section 4.2.1 (see Eq. 4.3). The plates are brought together and moved apart in an oscillatory manner, repeating periodically with period $\mathcal{T} = 0.5$. We recall that the initial pressure is constant and equal to $p_a = 0.1358$.

The time evolution of the pressure profile for one cycle of the squeeze motion is shown in Fig. 4.17 for viscoelastic lubricants. During the phase of separation of the plates, the cavitated region grows rapidly and there is no significant influence of viscoelasticity as a large fraction of the film lies within the mixture region, see

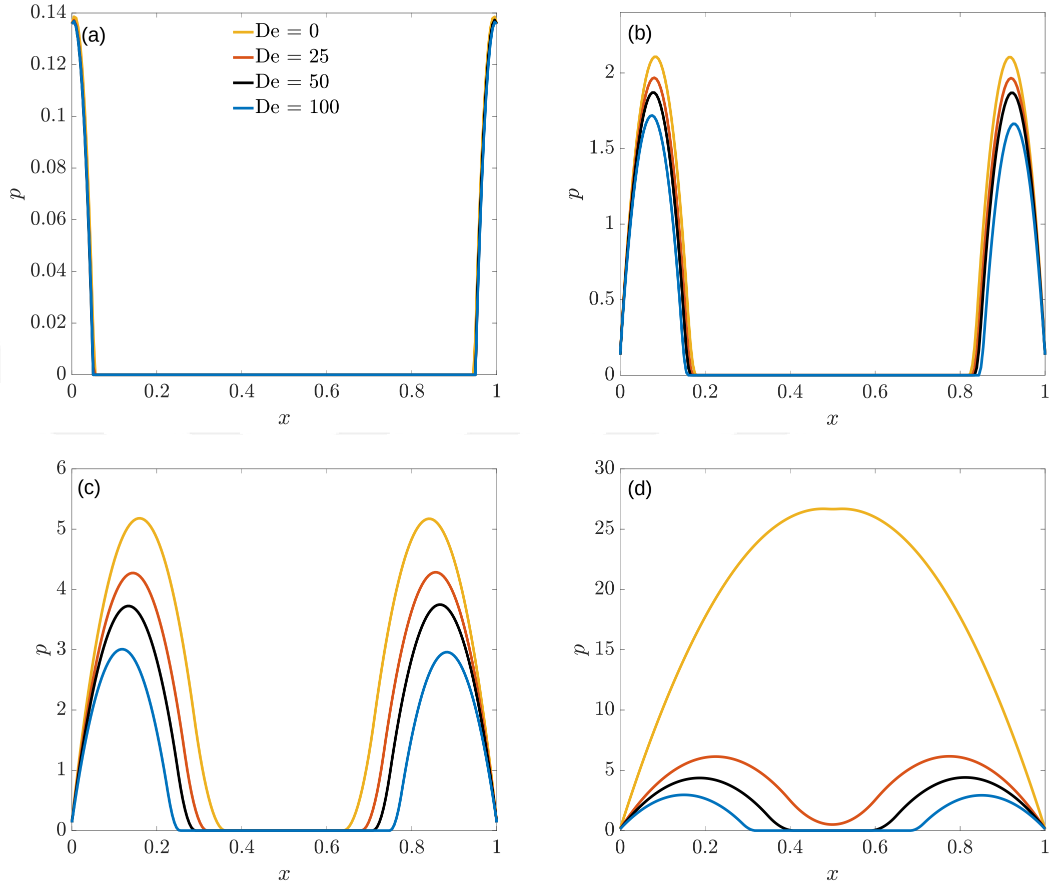

Figure 4.17: The time evolution of the pressure at (a) t = 1, (b) t = 1.2, (c) t = 1.22, and (d) t = 1.24 for $De = 0$ (yellow lines), $De = 25$ (red lines), $De = 50$ (black lines) and $De = 100$ (blue lines).

Fig. 4.17a at $t = 1$. As the plates are brought together, a gradual reformation of the film is observed (see Fig. 4.17b, for $t = 1.2$). The viscoelasticity is seen to reduce the maximum pressure. Fig. 4.17c (at $t = 1.22$) shows that the polymer addition also has a significant influence on the film reformation speed. As De increases the film reformation is much slower compared to a Newtonian lubricant. At $t = 1.24$ for low values of De, there is a brief period of complete film reformation before the cycle ends while, interestingly, full reformation does not re-occur before the end of the cycle if viscoelastic effects are strong (see Fig. 4.17d). Consequently, at large values of the Deborah number once the lubricant film has ruptured, a complete reformation is not observed anymore in the oscillatory squeezing of a viscoelastic lubricant.

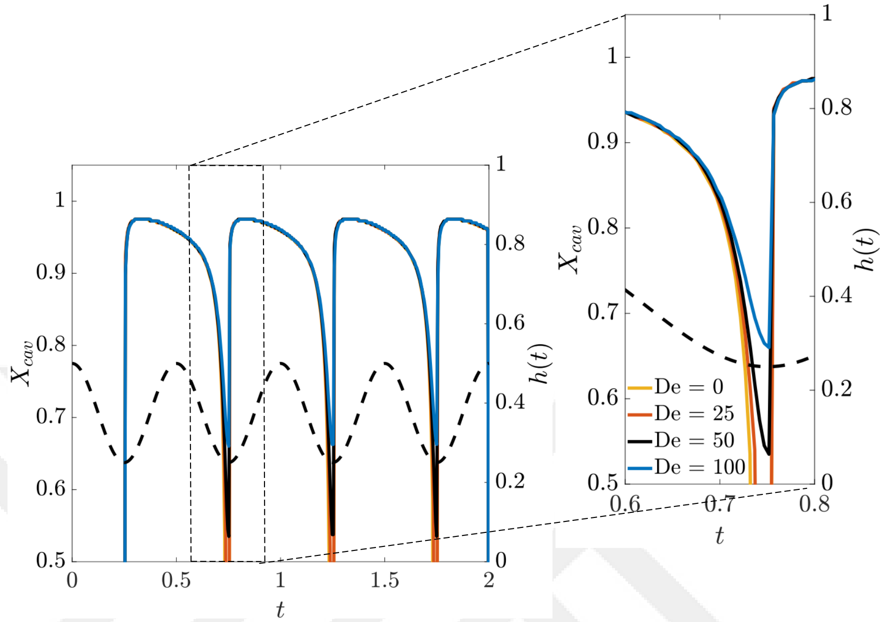

Figure 4.18: The location of the right cavitation boundary X_{cav} for various Deborah numbers.

We remember X_{cav} to be the right boundary of the cavitated region. Fig. 4.18 shows the temporal evolution of X_{cav} for different De values. Note that the dashed line represents the film height. We highlight the region between $t = 0.6$ and $t = 0.8$ where a complete reformation of the film is expected. In both Newtonian and viscoelastic lubricants, nucleation begins at $X_{cav} = 0.5$ when $t = 0.25$ (the time at which the surfaces begin to move apart). At a low De, the cavitation boundary X_{cav} is always included $0.5 \leq X_{cav} < 0.97$, if it does exist.

Deborah number	**Time at initial reform**	**Min.** $X_{cav}(t)$
0	0.366	0.50 (full reformation)
25	0.368	0.50 (full reformation)
50	0.370	0.51
75	0.372	0.59
100	0.374	0.64

Table 4.2: Cavitation data for the oscillatory squeeze flow for various Deborah numbers.

At large De, X_{cav} does not disappear anymore and it is always $X_{cav} > 0.5$ showing how a full-film reformation does not occur. In table 4.2 we report the (i) time at which the film begins to reform during the first cycle and (ii) the minimum value of X_{cav} for several Deborah numbers. At larger values of the Deborah number, there is an observable delay in the full-film reformation time which consequently results in a larger right cavitation boundary (X_{cav}).

The load for different Deborah numbers during the oscillatory squeeze flow is illustrated in Fig. 4.19. There is a significant variation in the load carrying capacity over time as a result of the phase transitions occurring within the lubricant film. This is expected since the top surface oscillates resulting in positive and negative squeezing. More interestingly, the total load decreases by increasing De. The maximum load is encountered just before negative squeezing begins, i.e before the inception of cavitation. At that moment the film thickness is minimum, the pressure is at its maximum and, as a consequence we have the smallest

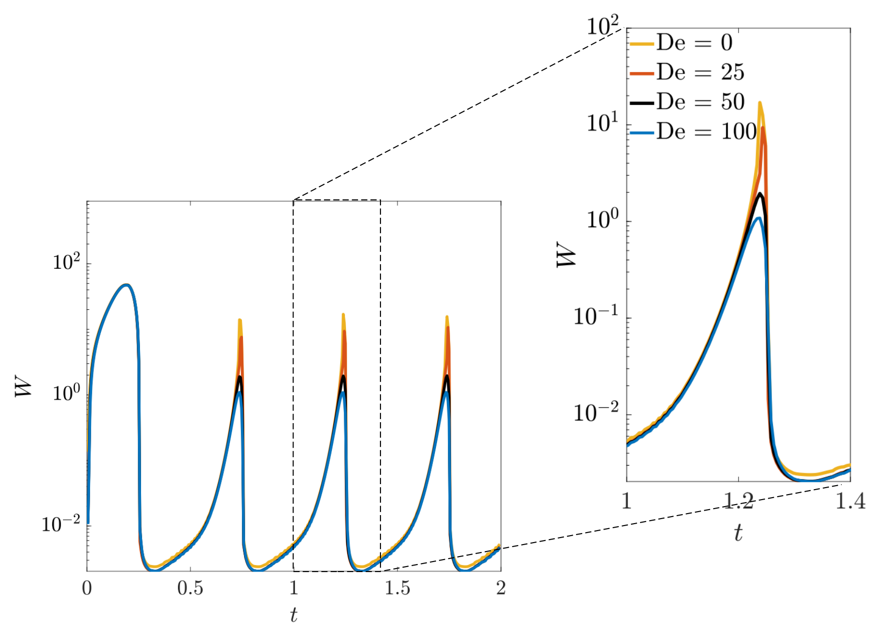

Figure 4.19: The load evolution in the squeeze film flow for different Deborah numbers.

non-active region. The load reduction reported in our proposed model can be attributed to the delayed film reformation observed in Fig. 4.17. Experiments, however, have shown that there is an increase in the load as viscoelastic effects are present [40]. To capture this load increase, the MPTT model presented by Phan-Thien et al. [15] has been reported to account for the stress overshoot in transient lubrication problems and shows an increase in the load for a single phase lubricant. We show in Appendix A that the linearization of the MPTT constitutive equation gives exactly the linearized Oldroyd-B model, i.e. Eqs. 3.8d-3.8f and Eqs. 3.9d-3.9f for the leading and first order terms, respectively. Consequently, the Oldroyd-B model remains a better option for easier modeling of the behavior of viscoelastic lubricants in the presence of cavitation.

Chapter 5

Direct Numerical Simulation

A more accurate tool based on Direct Numerical Simulation (DNS), can be used to describe the entire physics of the two fluids, by solving the Navier-Stokes equations, and their interaction. Previous works in literature have considered cavitation using both theoretical models [1],[27],[28] and DNS [29],[30]. In this chapter we make an attempt to put forward a DNS solver capable of predicting the viscoelastic effects in lubricants when cavitation is present by incorporating a viscoelastic fluid model with a multiphase solver.

A new solver capable of handling viscoelastic fluids with phase change is developed using the OpenFoam DNS tool. To obtain solutions using the two dimensional Navier-Stokes equations the problem is modeled using a combination of OpenFoam's interPhaseChangeFoam solver and rheotool's constitutive models. Rheotool's established constitutive equations include the Oldroyd-B, Giesekus, FENE-P, FENE-CR, exponential Phan-Thien-Tanner etc. In this work we shall incorporate the Oldroyd-B model into a multiphase solver which we call rheoPhaseFoam. The chapter is structured as follows, section 5.1 gives a brief introduction to the interPhaseChangeFoam and rheoInterFoam solver, alongside the features that will be taken from both solvers to form the rheoPhaseFoam solver. Section 5.2 highlights the equations to be solved by the rheoPhaseFoam solver and the mechanism of phase change adopted. A description of the numerical algorithm and simulation setup is made in section 5.3. In section 5.4 the results are presented and a discussion on the numerical instabilities associated with the solver is made in section 5.5.

5.1 RheoPhaseFoam

RheoPhaseFoam is the proposed numerical solver for viscoelastic fluids undergoing a phase change. This solver is developed as a hybrid case of OpenFoam's interPhaseChangeFoam solver and rheoTool's rheoInterFoam solver. For better understanding we make a brief introduction to both solvers below.

- **InterPhaseChangeFoam**
  This is a solver for two incompressible, isothermal immiscible fluids with phase change that incorporates the Volume of Fluid (VOF) phase-fraction based interface capturing approach [41, 42]. One momentum equation is solved which incorporates the fluid properties of the mixture. The Kunz, Merkle, and Schnerr-Sauer models [43] are utilized to simulate phase change, primarily for cavitation.

- **RheoInterFoam**
  The rheoInterFoam solver applies the transient, incompressible governing equations for two-phase flows of viscoelastic fluids using the Volume of Fluid (VOF) method to capture the interface. This solver solves the constitutive equation in each phase respectively and takes a weighted average of the extra-stress tensor contribution to the momentum equation for each phase. A Log-Conformal-Representation (LCR) is adapted into the model to transform the conformal tensor into a logarithmic variable and changes the polynomial difference schemes to an exponential form.

The rheoPhaseFoam solver is a transient solver for two incompressible, isothermal, immiscible and viscoelastic fluids with phase change occurring. The VOF method will be used to capture the interface between the two fluids. Here we introduce the volume fraction function α to determine the location of the interface and phase composition of two fluids within a control volume. For example in a liquid vapor mixture two phase flow, $\alpha = 1$ denotes a liquid phase and $\alpha = 0$ a vapor phase. Cells which lie between 0 and 1 are at the interface and mixture regions.

5.2 Governing equations

The governing equations for the rheoPhaseFoam solver are

(i) Continuity equation

$$\frac{\partial(\rho)}{\partial T} + \nabla \cdot (\rho \mathbf{u}) = 0, \tag{5.1}$$

(ii) Momentum conservation

$$\frac{\partial(\rho \mathbf{u})}{\partial t} + \nabla \cdot (\rho \mathbf{u}\mathbf{u}) = -\nabla P + \nabla \cdot \boldsymbol{\tau'} + \rho g + F_s, \tag{5.2}$$

(iii) Constitutive equation

$$f(\boldsymbol{\tau})\boldsymbol{\tau} + \lambda\hat{\boldsymbol{\tau}} + \boldsymbol{h(\tau)} = \eta_p(\nabla \boldsymbol{u} + \nabla \boldsymbol{u}^T), \tag{5.3}$$

(iv) VOF transport equation

$$\frac{\partial \alpha}{\partial T} + \nabla \cdot \alpha \mathbf{u} + \nabla \cdot (\alpha(1-\alpha)\boldsymbol{Ur_i}) = \dot{m}^+ + \dot{m}^-. \tag{5.4}$$

where $\mathbf{u}$ is the velocity vector, T is the time, ρ is the density, p is the pressure, $\boldsymbol{\tau'}$ is the extra stress tensor, α is the volume phase fraction, g is the acceleration due to gravity, $\boldsymbol{h(\tau)}$ is a tensor valued function depending on $\boldsymbol{\tau}$, F_s is any external body force and λ is the relaxation time. The total extra stress tensor is made up of the solvent contribution ($\boldsymbol{\tau}_s$) and a polymeric contribution ($\boldsymbol{\tau}$).

$$\boldsymbol{\tau'} = \boldsymbol{\tau} + \boldsymbol{\tau}_s, \tag{5.5}$$

with

$$\boldsymbol{\tau}_s = \eta_s(\nabla \boldsymbol{u} + \nabla \boldsymbol{u}^T), \tag{5.6}$$

The Oldroyd-B constitutive model is considered in this formulation, the constitutive equation can then be simplified to become

$$\boldsymbol{\tau} + \lambda \hat{\boldsymbol{\tau}} = \eta_p(\nabla \boldsymbol{u} + \nabla \boldsymbol{u}^T), \tag{5.7}$$

where $\hat{\boldsymbol{\tau}}$ represents the upper-convected time derivative and is given as

$$\hat{\boldsymbol{\tau}} = \frac{\partial \boldsymbol{\tau}}{\partial T} + \mathbf{u} \cdot \nabla \boldsymbol{\tau} - \boldsymbol{\tau} \cdot \nabla \mathbf{u} - \nabla \boldsymbol{u}^T \cdot \boldsymbol{\tau}. \tag{5.8}$$

The VOF transport equation (Eq. 5.4) has been modified to account for the phase transition and the resulting transport equation. The terms $\dot{m}^+$ and $\dot{m}^-$ represent the rate of mass flow from one phase to another. Condensation is represented by the positive term $\dot{m}^+$ whereas evaporation is expressed as the negative term $\dot{m}^-$. The mass transfer terms are obtained from the phase transition models (Merkle, Kunz or SchnerrSauer) [43]. The standard advection schemes have too much dispersion so an artificial compression is introduced to preserve the jump in α. The term $\boldsymbol{Ur_i}$ is a velocity field suitable to compress the interface. This term is only active at the interface region. The density and viscosity parameters are of the mixture and are determined accordingly using the two phase properties equations.

$$\rho \; = \; \alpha \rho_l \; + (1 - \alpha) \, \rho_v, \tag{5.9}$$

and

$$\mu \; = \; \alpha \mu_l \; + (1 - \alpha) \, \mu_v. \tag{5.10}$$

where ρ_l is the liquid density, ρ_v is the vapor density, μ_l is the liquid viscosity and μ_v is the vapor viscosity.

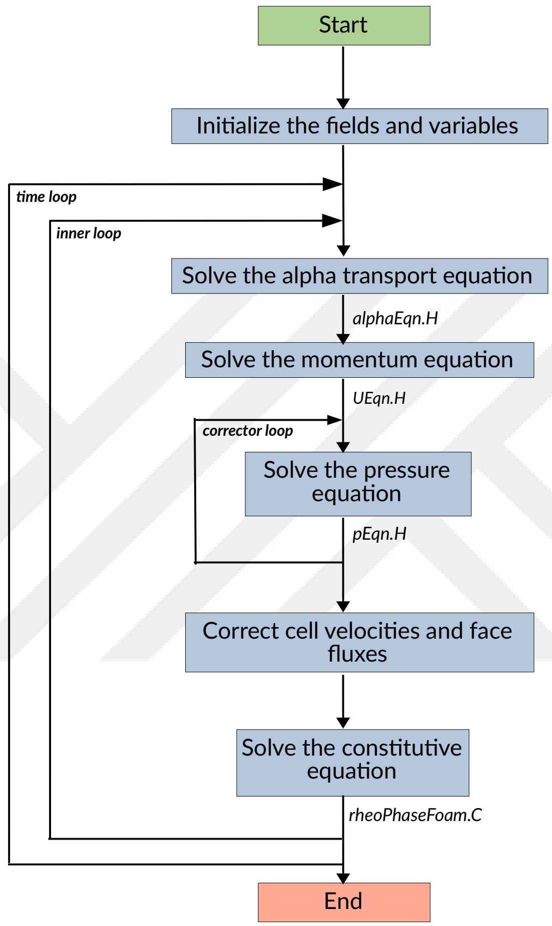

Figure 5.1: Schematic representation of the rheoPhaseFoam solver algorithm.

5.3 Numerical algorithm and setup

The solution algorithm is based on the PIMPLE algorithm originally used in the interPhaseChangeFoam solver. The solver starts by reading the initial variables and time controls. This is followed by a setting up of the respective fields and variables to be used within the solver. The time-step is adjusted depending on the CFL condition. The solver enters the time and inner loops to solve the alpha transport equation (alphaEqn.H). Based on the given alpha values around the mesh and the phase change model, the VOF transport model is solved in the alpha loop and the flux is determined. This is followed by a solution of the momentum equation (UEqn.H) where a tensor is created for the solution of $\mathbf{u}$ taking source terms from the phase change models. Next the pressure equation (pEqn.H) is solved within the pressure corrector loop and the velocity field is updated using the updated pressure field. A solution for the constitutive equation can then be reached using the updated velocity field. Once completed, the time step is increased and the loop returns to the top and solves for the next time step. A schematic drawing of the solver algorithm structure is shown in Fig. 5.1.

Time derivatives have been discretized using the Euler scheme. The convective terms were discretized using the linear upwind scheme [44]. The linear sets of equations were solved using the conjugated gradient method. The preconditioned bi-conjugate gradient stabilized method (BiCG) with a diagonal incomplete lower-upper (DILU) preconditioning was used for the velocity and stress, whereas pressure was solved with GAMG preconditioning. The absolute tolerance for the pressure, velocity and stresses were set to 10^{-10}. A solution criterion was set so that convergence was reached when the time T was beyond $T = 0.002s$ and the pressure residual was less than $tolerance = 10^{-8}$. The pressure residual was calculated using

$$residual = max\left[\frac{|p_{ij}^{t+\Delta t} - p_{ij}^{t}|}{|p_{ij}^{t}|}\right]. \tag{5.11}$$

The entire geometry, meshes and time steps have been chosen to induce the slightest cavitation while ensuring minimum spatial and temporal errors.

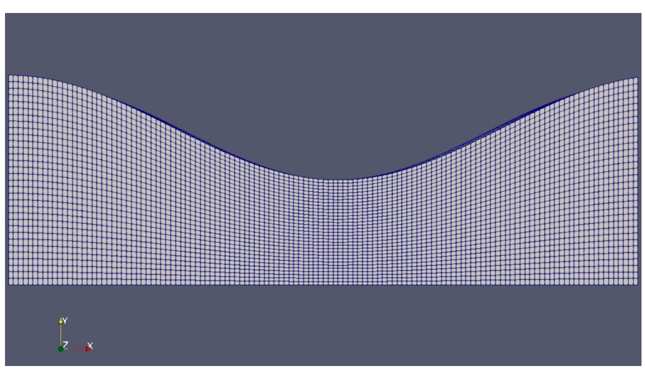

Figure 5.2: Cosine geometry showing the grid lines for the simulations.

5.3.1 Grid and domain

Simulations were carried out on a uniform grid for the cosine slider geometry (see Fig. 5.2). The simulation consists of four boundary patches; the inlet, outlet, a moving bottom surface and a stationary top surface. The maximum film thickness is located at both inlet and outlet surfaces whereas the minimum thickness is

N_x	N_y	Δx	Δy	ΔT
128	32	$\frac{L_x}{N_x}$	$\frac{H(x)}{N_y}$	10^{-10}

Table 5.1: Mesh data and initial time step.

located at the center of this configuration. The nodes are spaced equally in the x-direction and are unequally spaced in the y-direction due to the curvilinear domain. The domain configuration for this simulation has been used earlier and is described by Eq. 2.33. The corresponding configuration parameters and fluid properties have been tabulated in table 5.2.

Parameter	**Value**
Maximum Height $[m]$	$5.08 * 10^{-4}$
Minimum Height $[m]$	$2.54 * 10^{-4}$
Velocity $[m/s]$	4.57
Length $[m]$	0.0762
Liquid viscosity $[Pa \cdot s]$	0.039
Liquid density $[kg/m^3]$	1000
Vapor viscosity $[m^2/s]$	$4.273 * 10^{-4}$
Vapor density $[kg/m^3]$	0.02308
Saturation pressure $[Pa]$	2300
Lubricant surface tension $[kg/s^2]$	0.07

Table 5.2: Configuration parameters and values.

5.3.2 Boundary conditions

A constant velocity is applied to move the bottom surface whereas the top surface is in a fixed position. The velocities at the inlet and outlet are allowed to vary along with the flow. Pressures at the inlet and outlet remain at ambient pressure conditions and a full liquid film fraction condition is set at the inlet of the channel. Table 5.3 contains a more complete and comprehensive form of the boundary

Parameter	**Inlet**	**Outlet**	**Top**	**Bottom**
Velocity	$\frac{\partial u}{\partial n} = 0$	$\frac{\partial u}{\partial n} = 0$	no slip	$4.57m/s$
Volume fraction	$\alpha = 1$	$\alpha = 1$	$\frac{\partial \alpha}{\partial n} = 0$	$\frac{\partial \alpha}{\partial n} = 0$
Pressure	$2300Pa$	$2300Pa$	$\frac{\partial p}{\partial n} = 0$	$\frac{\partial p}{\partial n} = 0$

Table 5.3: Boundary conditions.

condition used for the simulations. The zero gradient boundary condition assumes that the derivative of a quantity along the normal direction to the boundary patch is zero, in this case

$$\frac{\partial u}{\partial n} = 0, \quad \frac{\partial v}{\partial n} = 0, \quad \frac{\partial p}{\partial n} = 0, \quad \text{and} \quad \frac{\partial \theta}{\partial n}. \tag{5.12}$$

5.4 Results

The rheoPhaseFoam solver has been used to obtain results for simulations using the configuration described in section 5.3. Results obtained were compared with solutions from the theoretical formulation proposed for when $De = 0$ and $De = 5$. The solvent concentration β was set to $\beta = 0.8$ for all the simulations reported in this chapter. The velocity contour from DNS results is displayed in Fig. 5.3a alongside the cosine geometry. Pressure and volume fraction contours are also shown in Fig. 5.3b and Fig. 5.3c respectively.

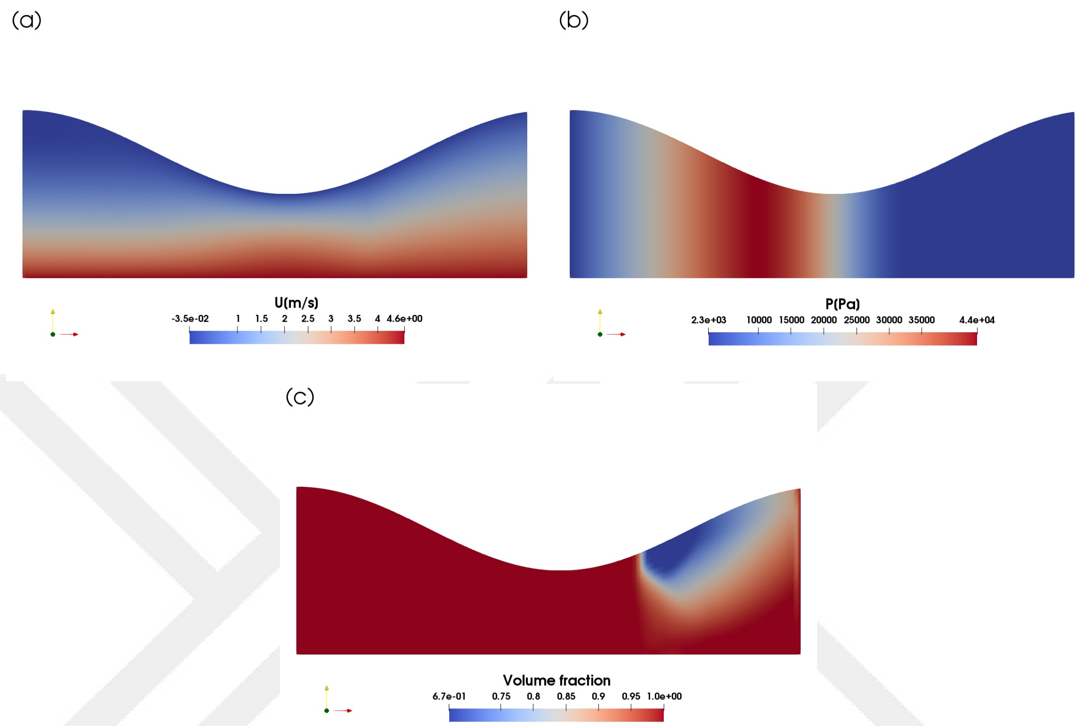

Figure 5.3: (a) Velocity contour (b) pressure contour, and (c) volume fraction in the cosine slider bearing solved using rheoPhaseFoam at $De = 5$.

The pressure distribution is shown in Fig. 5.4 comparing solutions from direct numerical simulations and the theoretical formulation postulated in section 3.6.1. DNS results show an increase in the maximum pressure with increasing viscoelastic effects in the cosine slider, a similar trend to what has been observed in theoretical results. The maximum pressure from DNS overestimates by 0.53% the maximum pressure obtained from theoretical results. The slight discrepancy observed between the pressure distribution for theoretical results compared to data from the numerical simulation can be attributed to the differences in how both models approach the problem. One major difference is that the theoretical solution uses a homogeneous mixture whereas DNS considers a vapor region with an interface between both fluids.

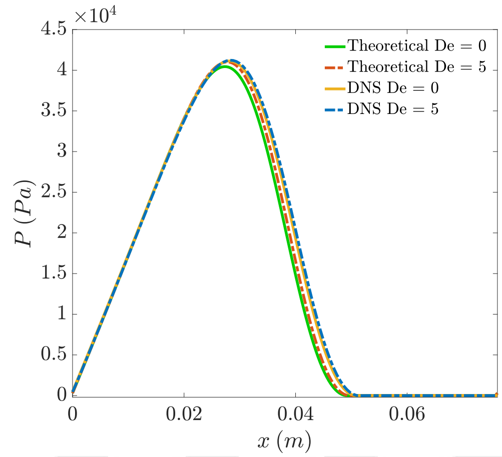

Figure 5.4: Pressure distribution comparing DNS and theoretical results in a cosine slider.

5.5 Numerical complexities

There are numerical instabilities arising from the outlet boundary condition which is seen to be insufficient for the incompressible solver. It has been observed that beyond certain values of the volume fraction there exist oscillations at the outlet section of the channel. While both the pressure and volume fraction seem to reach steady state, there are observable oscillations in the y-component of the velocity close to the outlet. Biancofiore et al. [45] suggested a sponge outflow boundary condition as a possible approach to eliminate these numerical oscillations at the outlet section.

At larger Deborah numbers, huge oscillations were observed for the simulations. Direct numerical simulation couples the Navier-Stokes equations with the constitutive equation in a non-linear manner. Due to this coupling there exists a non-linear instability arising. This is referred to as the High Deborah Number Problem (HDNP) which ensues at larger values of De. The term large here is relative and has been described by Ahmed and Biancofiore to vary with the nature of the problem [11]. Fattal et al. describe a failure of the polynomial based numerical schemes in capturing the exponential stress gradients as a cause of these instabilities [46]. This results in a high stress growth rate and an inhibition of the advective terms from removing stress effectively and thus causing a lack of convergence at larger Deborah numbers.

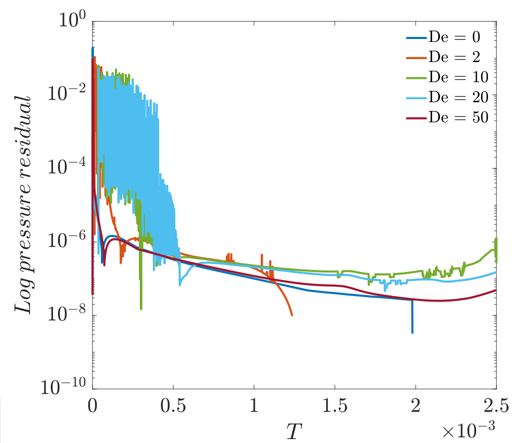

Figure 5.5: Pressure residual for several values of De.

Due to this numerical complexity, only low order models for viscoelastic lubricants can be found in literature and as such will be considered here. A log plot of the pressure residuals is shown in Fig. 5.5. Large oscillations are observed at higher values of De, and simulations are shown to converge only at lower De values. At much higher values of De, large oscillations were observed and this was followed by a divergence from the solution.

The Log-Conformal-Representation (LCR) has been adapted into the solver as a solution to the high Deborah number problem. It transforms the conformal tensor into a logarithmic variable used in converting the ordinary polynomial difference schemes to an exponential one. Although the LCR delays effects of the HDNP, this problem persists. Nevertheless the LCR has proven somewhat effective as it would be impossible to reach the results reported at $De = 5$ without this approach. The reader is referred to the work of the authors for a detailed analysis of the numerical schemes, discretization and performance of the technique [47, 48, 49].

Chapter 6

Conclusions

6.1 Summary

The addition of polymer additives to improve the overall performance of lubricants has become a common practice. The lubricants mechanical properties are altered due to the addition of polymers and they become viscoelastic. There has been experimental and numerical evidence to show that these viscoelastic lubricants exhibit better load enhancement properties [5, 50]. Previous formulations have however failed to account for the presence of cavitation and these models remain somewhat invalid for lubricant channels when cavitation is present. In this work, a model has been proposed to investigate effects of the presence of cavitation in viscoelastic lubricants. This is the first time that viscoelasticity of lubricants has been coupled with the presence of cavitation and studied to understand its influence in fluid film bearings.

The lubrication problem was studied in viscoelastic lubricants where the presence of cavitation was neglected. These studies showed that in regions where cavitation was known to occur, the generalized Reynolds equation reported negative pressures, indicating the fluid in that region was under tension. These models failed to properly describe the presence of the non-active region. Consequently, a more robust model for viscoelastic flows in lubricated contacts when cavitation is present has been proposed. The viscoelastic model that has been proposed is based on the Oldroyd-B constitutive relation. To achieve this, a linearization approach has been taken, using ϵDe as the perturbation parameter following the footsteps of Tichy [8].

Cavitation has been introduced to our proposed model using the mass conserving Elrod-Adams algorithm. This formulation incorporates the Jakobsson Floberg Olsson (JFO) theory with the following key objectives; (i) to remove the pressure contribution of the mass flow in the cavitation region, (ii) preserve the conservation of mass, and (iii) to set approximately correct conditions at cavitation boundaries. This produces a single equation applicable to both full film and cavitated regions. Properly accounting for the presence of cavitation in viscoelastic lubricants was expected to have an effect on the cavitation region. To capture these changes, a new set of boundary conditions at the interfaces between active and non-active regions have been proposed.

Profiles mimicking an unwrapped journal bearing and a surface texture have been considered for a pure sliding configuration. At higher Deborah numbers, it was shown that the load carrying capacity of the parabolic and twin parabolic profiles increase whereas there is an observed shrinking of the cavitation region. In a surface textured bearing, it has been observed that viscoelastic effects in the lubricant film is highly dependent on the location of the pocket. Load was shown to rapidly decrease with increasing values of De for a pocket located close to the channel inlet. There is a reported increase in the load with increasing viscoelastic effects when (i) the pocket is located in the middle or close to the exit and (ii) for a multi-pocketed profile. In addition results showed that friction is almost insensitive to viscoelasticity affirming the advantage of introducing polymers without causing additional losses due to interactions with the walls. The proposed model predicts well the location of the cavitation boundaries for the observed effects in the lubrication processes. The superiority of the introduced model stems from its easy implementation, particularly with the presence of cavitation well defined. A non-linear approach able to accurately predict the presence of cavitation will be a lot more difficult to implement.

To study the effect of polymer additives in the squeezing problem, two flat surfaces in oscillatory motion have been analyzed. There is an observable reduction in the maximum pressure of the lubricant with increasing viscoelastic effects. The rate of reformation of the viscoelastic lubricant film was slower compared to a Newtonian case. When viscoelastic effects become very strong, results show that after the initial rupture, the viscoelastic lubricant does not return to a complete liquid film. The results also suggest that load carrying capacities in the squeeze flow problem reduces with increasing values of De. A maximum load was shown to occur when the surfaces were at a point of minimum separation.

Results from previous experiments have reported that the load carrying capacity in squeezing films should show an increase with increasing viscoelastic effects [14]. On the other hand, works using the Oldroyd-B (or upper convective Maxwell) model showed a similar trend to what has been reported by our model [51]. Using the MPTT model, a load increase was reported and was in agreement with the experiments [15]. It was shown that the difference in results was due to the fact that MPTT model is taking into account the polymer stress overshoot which has not been considered by other models including the Oldroyd-B constitutive model. An attempt has been made with the MPTT model, however a linearization approach is seen to not be suitable for the MPTT model. This is as a result of the second order terms getting lost and the model is reduced to the original linearized Oldroyd-B model (see Appendix A).

Studies on the influence of viscoelastic lubricants when cavitation is present has been extended to direct numerical simulation. A solver for an incompressible, isothermal, viscoelastic, two phase fluid has been proposed. The solver was developed using the openFoam DNS tool by coupling a multi-phase flow solver with a viscoelastic solver from the rheoTool library. Results show that there is an increase in the maximum pressure with increasing viscoelastic effects as reported in our proposed theoretical solution. Slight variations in results have been attributed to differences between both models especially since the theoretical model considers a homogeneous mixture whereas DNS defines a vapor region with an interface between both fluids. Furthermore, viscoelastic effects have only been considered for very low values of De as a result of the large oscillations being observed at higher values of De. This problem is termed the high Deborah number problem (HDNP) and results from the inability of advective terms in removing the fast growing stresses effectively at larger values of De.

6.2 Perspectives

The proposed theoretical model makes a good prediction of the location of cavitation boundaries for the steady state lubrication process. Nevertheless, the polymer stress overshoot in the MPTT model cannot be neglected for transient problems as the polymer stress overshoot term becomes a critical factor in obtaining more accurate results. Considering a non-linear approach presents a better option for including the polymer stress overshoot term. One of such non-linear approaches is the generalized Reynolds equation [10] or the viscoelastic Reynolds equation, recently proposed by Ahmed and Biancofiore [11]. Including cavitation to the previously cited non-linear models will lead to a more robust model for viscoelastic lubricants.

Several attempts have been made to extend the modeling of viscoelastic effects on lubricants when cavitation is present using direct numerical simulation. Works by Hartinger et al. [52] and more recently Hajishafiee et al. [30] have developed a DNS solver for studying compressible elastohydrodynamic lubrication in roller bearings considering the influence when cavitation is present. More recently, Ahmed and Biancofiore [11] developed a novel DNS model based on the finite volume method [53] which can be used to study mild viscoelastic effects in lubricants. There is a need to further develop more numerically stable DNS approaches to account for the presence of cavitation in viscoelastic lubricants. For instance, a DNS model capable of coupling the numerical models developed by Ahmed and Biancofiore [11] and the algorithm proposed by Hijashafiee [30], will be very promising and effective towards describing cavitation in viscoelastic films.

Further developments could be made to include studies on the effect of temperature changes in fluid film bearings where cavitation is present. In addition, modeling the deformation of solid surfaces will be an interesting development to the models presented in this thesis.

Appendix A

Linearization of the MPTT model

In this Appendix our aim is to (i) introduce the MPTT model and (ii) linearize it taking ϵDe as the perturbation parameter. The modified Phan Thien Tanner (MPTT) constitutive model has been developed to take into account the stress overshoot experienced in squeeze flow problems which reported results with a similar trend to experimental results [15]. The governing equations for the MPTT constitutive relation is

$$f\left(tr\left(\boldsymbol{\tau}\right)\right)\boldsymbol{\tau} + \lambda\left(\frac{\partial \boldsymbol{\tau}}{\partial t} + \boldsymbol{u}\cdot\nabla\boldsymbol{\tau} - \left(\nabla\boldsymbol{u}\right)\cdot\boldsymbol{\tau} - \boldsymbol{\tau}\cdot\left(\nabla\boldsymbol{u}\right)^{T}\right) = 2\eta_m\boldsymbol{D}, \tag{A.1}$$

where $f\left(tr\left(\boldsymbol{\tau}\right)\right)$ depends on the stress tensor, and can be defined either as an exponential function

$$f\left(tr\left(\boldsymbol{\tau}\right)\right) = exp\left(\frac{q\lambda}{\eta_p}tr\left(\boldsymbol{\tau}\right)\right), \tag{A.2}$$

or the linear PTT model which will be used in this paper

$$f\left(tr\left(\boldsymbol{\tau}\right)\right) = 1 + \frac{q\lambda}{\eta_p}tr\left(\boldsymbol{\tau}\right), \tag{A.3}$$

where, q is inversely proportional to the extensional viscosity of the fluid and

$$\eta_m = \eta_p\frac{1+\zeta(2-\zeta)\lambda^2\dot{\gamma}^2}{(1+\Gamma^2\dot{\gamma}^2)^{(1-n)/2}}. \tag{A.4}$$

Note that in Eq. A.4, Γ is a time parameter, n is the power-law index, ζ is the overshoot parameter, and $\dot{\gamma}^2 = 2tr\boldsymbol{D}^2$ is the generalized shear rate. The constitutive equation can be rewritten in the form

$$f\left(tr\left(\boldsymbol{\tau}\right)\right)\boldsymbol{\tau} + \lambda\left(\frac{\partial \boldsymbol{\tau}}{\partial t} + \boldsymbol{v}\cdot\nabla\boldsymbol{\tau} - \left(\nabla\boldsymbol{v}\right)\cdot\boldsymbol{\tau} - \boldsymbol{\tau}\cdot\left(\nabla\boldsymbol{v}\right)^T\right) = 2\mu(1-\beta)\eta\boldsymbol{D}, \quad \text{(A.5)}$$

where

$$\mu = \frac{1+\zeta(2-\zeta)\lambda^2\dot{\gamma}^2}{(1+\Gamma^2\dot{\gamma}^2)^{(1-n)/2}}. \quad \text{(A.6)}$$

Applying the thin film approximation with the non-dimensional parameters introduced in section 3.3, the constitutive equations become expressed in the scalar form

$$\tau_{xx} + \epsilon De\left(\frac{\partial \tau_{xx}}{\partial t} + u_x\frac{\partial \tau_{xx}}{\partial x} + u_y\frac{\partial \tau_{xx}}{\partial y} - 2\frac{\partial u_x}{\partial y}\tau_{xy} - 2\frac{\partial u_x}{\partial x}\tau_{xx}\right) = \\ -2\frac{\partial u_x}{\partial x}\epsilon^2(1-\beta)\left[\frac{1+2\zeta(2-\zeta)\epsilon^2De^2\frac{\partial u_x}{\partial x}^2}{\left(1+2\epsilon^2De^2\frac{\partial u_x}{\partial x}^2\right)^{\frac{1-n}{2}}}\right], \quad \text{(A.7a)}$$

$$\tau_{xy} + \epsilon De\left(\frac{\partial \tau_{xy}}{\partial t} + u_x\frac{\partial \tau_{xy}}{\partial x} + u_y\frac{\partial \tau_{xy}}{\partial y} - \frac{\partial u_x}{\partial y}\tau_{yy} - \frac{\partial u_y}{\partial x}\tau_{xx}\right) = \\ -(1-\beta)\left(\frac{\partial u_x}{\partial y} + \frac{\partial u_y}{\partial x}\epsilon^2\right)\left[\frac{1+2\zeta(2-\zeta)\epsilon^2De^2\left(\frac{\partial u_x}{\partial y}\frac{L}{H_0} + \frac{\partial u_y}{\partial x}\frac{H_0}{L}\right)^2}{\left[1+2\epsilon^2De^2\left(\frac{\partial u_x}{\partial y}\frac{L}{H_0} + \frac{\partial u_y}{\partial x}\frac{H_0}{L}\right)^2\right]^{\frac{1-n}{2}}}\right], \text{ and} \quad \text{(A.7b)}$$

$$\tau_{yy} + \epsilon De\left(\frac{\partial \tau_{yy}}{\partial t} + u_x\frac{\partial \tau_{yy}}{\partial x} + u_y\frac{\partial \tau_{yy}}{\partial y} - 2\frac{\partial u_y}{\partial y}\tau_{yy} - 2\frac{\partial u_y}{\partial x}\tau_{xy}\right) = \\ -2(1-\beta)\frac{\partial u_y}{\partial y}\left[\frac{1+2\zeta(2-\zeta)\epsilon^2De^2\frac{\partial u_y}{\partial y}^2}{\left(1+2\epsilon^2De^2\frac{\partial u_y}{\partial y}^2\right)^{\frac{1-n}{2}}}\right]. \quad \text{(A.7c)}$$

Considering $\epsilon^2 \to 0$, the term on the right side of Eq. A.7a is lost and this reduces to the Oldroyd-B constitutive relation (Eq. 3.6d). The zeroth and first order ϵDe terms of Eqs. A.7a-A.7c are the same as the terms derived from the Oldroyd-B model (see section 3.4: Eqs. 3.8d-3.8f and Eqs. 3.9d-3.9f). This means that when second order terms in ϵDe are neglected, as has been done in this thesis, the linearized thin film equations of the MPTT and Oldroyd-B models are the same. Also, the parameter ζ can only be present for higher order terms of ϵDe, agreeing that the effect of the polymer stress overshoot cannot be described by the linearized model.

All the terms containing De^2 on the right side of Eq. A.7b and Eq. A.7c vanish and the equations can be written as Eq. 3.6e and Eq. 3.6f respectively. It is important to note that for the linearized MPTT model, the terms on the right hand side of the constitutive equations are either on the order of ϵ, De^2 or larger. The De^2 terms are

$$\frac{\partial \tau_{xx}^D}{\partial t}+u_x^L\frac{\partial \tau_{xx}^D}{\partial x}+u_x^D\frac{\partial \tau_{xx}^L}{\partial x}+u_y^L\frac{\partial \tau_{xx}^D}{\partial y}+u_y^D\frac{\partial \tau_{xx}^L}{\partial y}-2\frac{\partial u_x^D}{\partial y}\tau_{xy}^L-2\frac{\partial u_x^L}{\partial y}\tau_{xy}^D-2\frac{\partial u_x^D}{\partial x}\tau_{xx}^L-2\frac{\partial u_x^L}{\partial x}\tau_{xx}^D=0, \tag{A.8a}$$

$$\frac{\partial \tau_{xy}^D}{\partial t}+u_x^L\frac{\partial \tau_{xy}^D}{\partial x}+u_x^D\frac{\partial \tau_{xy}^L}{\partial x}+u_y^L\frac{\partial \tau_{xy}^D}{\partial y}+u_y^D\frac{\partial \tau_{xy}^L}{\partial y}-\frac{\partial u_x^D}{\partial y}\tau_{yy}^L-\frac{\partial u_x^L}{\partial y}\tau_{yy}^D-\frac{\partial u_y^D}{\partial x}\tau_{xx}^L-\frac{\partial u_y^L}{\partial x}\tau_{xx}^D=$$
$$-\delta\frac{\partial u_x^L}{\partial y}\left[\frac{1+2\zeta(2-\zeta)\epsilon^2De^2\left(\frac{\partial u_x^L}{\partial y}\frac{1}{\epsilon}+\frac{\partial u_y^L}{\partial x}\epsilon\right)^2}{\left[1+2\epsilon^2De^2\left(\frac{\partial u_x^L}{\partial y}\frac{1}{\epsilon}+\frac{\partial u_y^L}{\partial x}\epsilon\right)^2\right]^{\frac{1-n}{2}}}\right], \text{ and} \tag{A.8b}$$

$$\frac{\partial \tau_{yy}^D}{\partial t}+u_x^L\frac{\partial \tau_{yy}^D}{\partial x}+u_x^D\frac{\partial \tau_{yy}^L}{\partial x}+u_y^L\frac{\partial \tau_{yy}^D}{\partial y}+u_y^D\frac{\partial \tau_{yy}^L}{\partial y}-2\frac{\partial u_y^D}{\partial y}\tau_{yy}^L-2\frac{\partial u_y^L}{\partial y}\tau_{yy}^D-2\frac{\partial u_y^D}{\partial x}\tau_{xy}^L-2\frac{\partial u_y^L}{\partial x}\tau_{xy}^D=$$
$$-2\delta\frac{\partial u_y^L}{\partial y}\left[\frac{1+2\zeta(2-\zeta)\epsilon^2De^2\frac{\partial u_y^L}{\partial y}^2}{\left(1+2\epsilon^2De^2\frac{\partial u_y^L}{\partial y}^2\right)^{\frac{1-n}{2}}}\right]. \tag{A.8c}$$

ζ vanishes with the De^2 terms and so therefore these terms cannot be neglected. To include the stress overshoot effects, the higher order terms need to be taken into account. For a linearization approach using ϵDe as the perturbation parameter, the MPTT model reduces to the Oldroyd-B model. This is as a result of the second order terms arising in the MPTT term shown in Eq. (A.6).

This formulation can be applied to other constitutive models by taking into consideration that for

- Newtonian model: $n = 1,\ \lambda = 0,\ q = 0,\ \beta = 1$ and $\zeta = 0$
- Oldroyd-B model: $n = 1,\ q = 0, 0 < \beta < 1,\ \eta = \eta_m = \eta_p$ and $\zeta = 0$
- upper-convected Maxwell model: $n = 1,\ q = 0,\ \beta = 0,\ \eta = \eta_m = \eta_p$ and $\zeta = 0$
- PTT model: $\beta = 0,\ \eta = \eta_m = \eta_p,\ n = 1$ and $\zeta = 0$.

Appendix B

Thin film approximation

In this Appendix, we carry out a more detailed analysis on the reduction of the equations for the Oldroyd-B constitutive model through a lubrication approximation, i.e. the parameter $\epsilon << 1$. To do so, the non-dimensional parameters introduced in section 3.3 are substituted into the Navier-Stokes equations (Eqs. 3.1 and 3.2) and the Oldroyd-B constitutive equations (Eq. 3.3). The resulting set of non-dimensional equations become

$$\frac{\partial \theta}{\partial t} + \frac{\partial \left(\theta u_x\right)}{\partial x} + \frac{\partial \left(\theta u_y\right)}{\partial y} = 0, \tag{B.1a}$$

$$\epsilon \, Re \, \theta \, \rho_l \left(\frac{\partial u_x}{\partial t} + u_x \frac{\partial u_x}{\partial x} + u_y \frac{\partial u_x}{\partial y} \right) = \frac{\partial \tau_{xx}}{\partial x} + \frac{\partial \tau_{xy}}{\partial y} + \epsilon \frac{\partial^2 u_x}{\partial x^2} + \beta \frac{\partial^2 u_x}{\partial y^2} + \frac{\partial p}{\partial x}, \tag{B.1b}$$

$$\epsilon \, Re \, \theta \, \rho_l \left(\frac{\partial u_y}{\partial t} + u_x \frac{\partial u_y}{\partial x} + u_y \frac{\partial u_y}{\partial y} \right) = \epsilon \frac{\partial \tau_{xy}}{\partial x} + \epsilon \frac{\partial \tau_{yy}}{\partial y} + \epsilon \frac{\partial^2 u_y}{\partial x^2} + \epsilon \frac{\partial^2 u_y}{\partial y^2} + \frac{\partial p}{\partial y}, \tag{B.1c}$$

$$\tau_{xx} + \epsilon De \left(\frac{\partial \tau_{xx}}{\partial t} + u_x \frac{\partial \tau_{xx}}{\partial x} + u_y \frac{\partial \tau_{xx}}{\partial y} - 2 \frac{\partial u_x}{\partial y} \tau_{xy} - 2 \frac{\partial u_x}{\partial x} \tau_{xx} \right) = -2 \frac{\partial u_x}{\partial x} \epsilon^2 \beta, \tag{B.1d}$$

$$\tau_{xy} + \epsilon De\left(\frac{\partial \tau_{xy}}{\partial t} + u_x\frac{\partial \tau_{xy}}{\partial x} + u_y\frac{\partial \tau_{xy}}{\partial y} - \frac{\partial u_x}{\partial y}\tau_{yy} - \frac{\partial u_y}{\partial x}\tau_{xx}\right) = \\ -(1-\beta)\left(\frac{\partial u_x}{\partial y} + \frac{\partial u_y}{\partial x}\epsilon^2\right), \text{ and} \tag{B.1e}$$

$$\tau_{yy}+\epsilon De\left(\frac{\partial \tau_{yy}}{\partial t} + u_x\frac{\partial \tau_{yy}}{\partial x} + u_y\frac{\partial \tau_{yy}}{\partial y} - 2\frac{\partial u_y}{\partial y}\tau_{yy} - 2\frac{\partial u_y}{\partial x}\tau_{xy}\right) = -2(1-\beta)\frac{\partial u_y}{\partial y}. \tag{B.1f}$$

Note that in this formulation we have terms proportional to ϵDe. Due to our definition of the Deborah number (i.e. using H_{max} as reference scale), viscoelastic effects start to be relevant at large values of De. This means that the ϵDe-terms can no longer be neglected only because $\epsilon << 1$ [54]. Furthermore this can be used to justify our linearization using ϵDe as a perturbation parameter since these terms are smaller than the $O(1)$-terms in ϵ. Therefore, if $\epsilon << 1$, as assumed in the thin film approximation, Eqs. B.1 become Eqs. 3.6. It should be noted that the continuity equation (Eq. B.1a) remains unchanged since ϵ is not present.

Bibliography

[1] M. Giacopini, M. T. Fowell, D. Dini, and A. Strozzi, "A mass-conserving complementarity formulation to study lubricant films in the presence of cavitation," *Journal of tribology*, vol. 132, no. 4, 2010.

[2] R. F. Ausas, M. Jai, and G. C. Buscaglia, "A mass-conserving algorithm for dynamical lubrication problems with cavitation," *Journal of Tribology*, vol. 131, no. 3, 2009.

[3] S. T. Moeller, *Energy efficiency: issues and trends.* Nova Publishers, 2002.

[4] A. Z. Szeri, *Fluid film lubrication.* Cambridge university press, 2010.

[5] B. Williamson, K. Walters, T. Bates, R. Coy, and A. Milton, "The viscoelastic properties of multigrade oils and their effect on journal bearing characteristics," *Journal of Non-Newtonian Fluid Mechanics*, vol. 73, no. 1-2, pp. 115–126, 1997.

[6] A. Davies and X. Li, "Numerical modelling of pressure and temperature effects in viscoelastic flow between eccentrically rotating cylinders," *Journal of non-Newtonian fluid mechanics*, vol. 54, pp. 331–350, 1994.

[7] O. Reynolds, "Iv. on the theory of lubrication and its application to mr. beauchamp tower's experiments, including an experimental determination of the viscosity of olive oil," *Philosophical transactions of the Royal Society of London*, no. 177, pp. 157–234, 1886.

[8] J. Tichy, "Non-newtonian lubrication with the convected maxwell model," 1996.

[9] X. K. Li, "Non-newtonian lubrication with the phan-thien-tanner model," *Journal of Engineering Mathematics*, vol. 87, no. 1, pp. 1–17, 2014.

[10] R. Wolff and A. Kubo, "A generalized non-newtonian fluid model incorporated into elastohydrodynamic lubrication," 1996.

[11] H. Ahmed and L. Biancofiore, "An improved simplified model for viscoelastic thin-film lubrication," *Journal of non-Newtonian Fluid Mechanics*, p. submitted, 2020.

[12] N. Phan-Thien and R. Tanner, "Lubrication squeeze-film theory for the oldroyd-b fluid," *Journal of non-newtonian fluid mechanics*, vol. 14, pp. 327–335, 1984.

[13] N. Phan-Thien, J. Dudek, D. Boger, and V. Tirtaatmadja, "Squeeze film flow of ideal elastic liquids," *Journal of non-newtonian fluid mechanics*, vol. 18, no. 3, pp. 227–254, 1985.

[14] P. J. Leider and R. B. Bird, "Squeezing flow between parallel disks. i. theoretical analysis," *Industrial & Engineering Chemistry Fundamentals*, vol. 13, no. 4, pp. 336–341, 1974.

[15] N. Phan-Thien, F. Sugeng, and R. Tanner, "The squeeze-film flow of a viscoelastic fluid," *Journal of non-newtonian fluid mechanics*, vol. 24, no. 1, pp. 97–119, 1987.

[16] N. Phan-Thien and R. I. Tanner, "A new constitutive equation derived from network theory," *Journal of Non-Newtonian Fluid Mechanics*, vol. 2, no. 4, pp. 353–365, 1977.

[17] N. Phan-Thien and N. Mai-Duy, *Understanding viscoelasticity: an introduction to rheology.* Springer, 2017.

[18] M. Yousfi, B. Bou-Saïd, and J. Tichy, "An analytical study of the squeezing flow of synovial fluid," *Mechanics & Industry*, vol. 14, no. 1, pp. 59–69, 2013.

[19] L. Gümbel, "Das problem der lagerreibung," *Mbl. Berlin. Bez. Ver. dtsch. Ing*, vol. 5, pp. 87–104, 1914.

[20] H. W. Swift, “The stability of lubricating films in journal bearings.(includes appendix).,” in *Minutes of the Proceedings of the Institution of Civil Engineers*, vol. 233, pp. 267–288, Thomas Telford-ICE Virtual Library, 1932.

[21] W. Stieber and D. Schwimmlager, “Hydrodynamische theorie des gleitlagers,” 1933.

[22] B. Jakobsson, “The finite journal bearing, considering vaporization,” *Transactions of Chalmers University of Technology*, vol. 190, 1957.

[23] K.-O. Olsson, “Cavitation in dynamically loaded bearings,” *Transactions of Chalmers University of Technology*, vol. 308, 1965.

[24] H. Elrod, “A computer program for cavitation and starvation problems,” *Cavitation and related phenomena in lubrication*, vol. 37, 1974.

[25] S. Saprykin, R. J. Koopmans, and S. Kalliadasis, “Free-surface thin-film flows over topography: influence of inertia and viscoelasticity,” *Journal of Fluid Mechanics*, vol. 578, p. 271, 2007.

[26] M. Anand, J. Kwack, and A. Masud, “A new generalized oldroyd-b model for blood flow in complex geometries,” *International Journal of Engineering Science*, vol. 72, pp. 78–88, 2013.

[27] F. Sahlin, A. Almqvist, R. Larsson, and S. Glavatskih, “A cavitation algorithm for arbitrary lubricant compressibility,” *Tribology International*, vol. 40, no. 8, pp. 1294–1300, 2007.

[28] R. Ausas, P. Ragot, J. Leiva, M. Jai, G. Bayada, and G. C. Buscaglia, “The impact of the cavitation model in the analysis of microtextured lubricated journal bearings,” 2007.

[29] M. Hartinger, *CFD modelling of elastohydrodynamic lubrication*. PhD thesis, Department of Mechanical Engineering, Imperial College London 2007., 2007.

[30] A. Hajishafiee, A. Kadiric, S. Ioannides, and D. Dini, "A coupled finite-volume cfd solver for two-dimensional elasto-hydrodynamic lubrication problems with particular application to rolling element bearings," *Tribology International*, vol. 109, pp. 258–273, 2017.

[31] D. Vijayaraghavan and T. Keith Jr, "Development and evaluation of a cavitation algorithm," *Tribology Transactions*, vol. 32, no. 2, pp. 225–233, 1989.

[32] R. Tuomas and O. Isaksson, "Compressibility of oil/refrigerant lubricants in elasto-hydrodynamic contacts," 2006.

[33] H. G. Elrod, "A cavitation algorithm," 1981.

[34] J. Oldroyd, "Non-newtonian effects in steady motion of some idealized elastico-viscous liquids," *Proceedings of the Royal Society of London. Series A. Mathematical and Physical Sciences*, vol. 245, no. 1241, pp. 278–297, 1958.

[35] D. Trevena, "Cavitation and the generation of tension in liquids," *Journal of Physics D: Applied Physics*, vol. 17, no. 11, p. 2139, 1984.

[36] S.-C. Vladescu, A. V. Olver, I. G. Pegg, and T. Reddyhoff, "The effects of surface texture in reciprocating contacts–an experimental study," *Tribology International*, vol. 82, pp. 28–42, 2015.

[37] L. Biancofiore, M. Giacopini, and D. Dini, "Interplay between wall slip and cavitation: A complementary variable approach," *Tribology International*, vol. 137, pp. 324–339, 2019.

[38] V. Optasanu and D. Bonneau, "Finite element mass-conserving cavitation algorithm in pure squeeze motion. validation/application to a connecting-rod small end bearing," *J. Trib.*, vol. 122, no. 1, pp. 162–169, 2000.

[39] L. Bertocchi, D. Dini, M. Giacopini, M. T. Fowell, and A. Baldini, "Fluid film lubrication in the presence of cavitation: a mass-conserving two-dimensional formulation for compressible, piezoviscous and non-newtonian fluids," *Tribology International*, vol. 67, pp. 61–71, 2013.

[40] J. A. Tichy and W. O. Winer, "An investigation into the influence of fluid viscoelasticity in a squeeze film bearing," 1978.

[41] B. Nichols and C. Hirt, "Methods for calculating multidimensional, transient free surface flows past bodies," in *Proceedings of the 1st International Conference on Ship Hydrodynamics*, pp. 253–277, 1975.

[42] C. W. Hirt and B. D. Nichols, "Volume of fluid (vof) method for the dynamics of free boundaries," *Journal of computational physics*, vol. 39, no. 1, pp. 201–225, 1981.

[43] R. F. Kunz, D. A. Boger, D. R. Stinebring, T. S. Chyczewski, J. W. Lindau, H. J. Gibeling, S. Venkateswaran, and T. Govindan, "A preconditioned navier-stokes method for two-phase flows with application to cavitation prediction," *Computers & Fluids*, vol. 29, no. 8, pp. 849–875, 2000.

[44] J. Favero, A. Secchi, N. Cardozo, and H. Jasak, "Viscoelastic flow analysis using the software openfoam and differential constitutive equations," *Journal of non-Newtonian fluid mechanics*, vol. 165, no. 23-24, pp. 1625–1636, 2010.

[45] L. Biancofiore, F. Gallaire, and R. Pasquetti, "Influence of confinement on a two-dimensional wake," *Journal of fluid mechanics*, vol. 688, no. ARTICLE, pp. 297–320, 2011.

[46] R. Fattal and R. Kupferman, "Constitutive laws for the matrix-logarithm of the conformation tensor," *Journal of Non-Newtonian Fluid Mechanics*, vol. 123, no. 2-3, pp. 281–285, 2004.

[47] R. Fattal and R. Kupferman, "Time-dependent simulation of viscoelastic flows at high weissenberg number using the log-conformation representation," *Journal of Non-Newtonian Fluid Mechanics*, vol. 126, no. 1, pp. 23–37, 2005.

[48] H. Jasak, A. Jemcov, Z. Tukovic, *et al.*, "Openfoam: A c++ library for complex physics simulations," in *International workshop on coupled methods in numerical dynamics*, vol. 1000, pp. 1–20, IUC Dubrovnik Croatia, 2007.

[49] F. Habla, M. W. Tan, J. Haßlberger, and O. Hinrichsen, "Numerical simulation of the viscoelastic flow in a three-dimensional lid-driven cavity using the log-conformation reformulation in openfoam®," *Journal of Non-Newtonian Fluid Mechanics*, vol. 212, pp. 47–62, 2014.

[50] N. Phan-Thien and H. Low, "Squeeze-film flow of a viscoelastic fluid a lubrication model," *Journal of non-Newtonian fluid mechanics*, vol. 28, no. 2, pp. 129–148, 1988.

[51] N. Phan-Thien and R. Tanner, "Viscoelastic squeeze-film flows–maxwell fluids," *Journal of Fluid Mechanics*, vol. 129, pp. 265–281, 1983.

[52] M. Hartinger, D. Gosman, S. Ioannides, and H. A. Spikes, "Cfd modelling of elastohydrodynamic lubrication," in *World Tribology Congress*, vol. 42010, pp. 531–532, 2005.

[53] H. K. Versteeg and W. Malalasekera, *An introduction to computational fluid dynamics: the finite volume method*. Pearson education, 2007.

[54] F. T. Akyildiz and H. Bellout, "Viscoelastic lubrication with phan-thien-tanner fluid (ptt)," *J. Trib.*, vol. 126, no. 2, pp. 288–291, 2004.